NANO LETTERS

Letter

pubs.acs.org/NanoLett

InP Nanowire Biosensor with Tailored Biofunctionalization: Ultrasensitive and Highly Selective Disease Biomarker Detection

Richard Janissen,*[,†,‡] Prasana K. Sahoo,[†] Clelton A. Santos,[§] Aldeliane M. da Silva,[†] Antonio A. G. von Zuben,[†] Denio E. P. Souto,[∥] Alexandre D. T. Costa,[⊥] Paola Celedon,[#] Nilson I. T. Zanchin,[⊥] Diogo B. Almeida,[†] Douglas S. Oliveira,[†] Lauro T. Kubota,[∥] Carlos L. Cesar,[†] Anete P. de Souza,[§] and Monica A. Cotta*[,†]

[†]"Gleb Wataghin" Physics Institute, University of Campinas, Campinas, São Paulo 13083-859, Brazil

[‡]Kavli Institute of Nanoscience, Delft University of Technology, 2629 HZ Delft, The Netherlands

[§]Center for Molecular Biology and Genetic Engineering, Biology Institute, University of Campinas, Campinas, São Paulo 13083-875, Brazil

[∥]Chemistry Institute, University of Campinas, Campinas, São Paulo 13083-970, Brazil

[⊥]Oswaldo Cruz Foundation, Carlos Chagas Institute, Curitiba, Paraná 81310-020 Brazil

[#]Molecular Biology Institute of Paraná, Curitiba, Paraná 81310-020 Brazil

Supporting Information

ABSTRACT: Electrically active field-effect transistors (FET) based biosensors are of paramount importance in life science applications, as they offer direct, fast, and highly sensitive label-free detection capabilities of several biomolecules of specific interest. In this work, we report a detailed investigation on surface functionalization and covalent immobilization of biomarkers using biocompatible ethanolamine and poly-(ethylene glycol) derivate coatings, as compared to the conventional approaches using silica monoliths, in order to substantially increase both the sensitivity and molecular selectivity of nanowire-based FET biosensor platforms. Quantitative fluorescence, atomic and Kelvin probe force microscopy allowed detailed investigation of the homogeneity and density of immobilized biomarkers on different biofunctionalized surfaces. Significantly enhanced binding specificity, biomarker density, and target biomolecule capture efficiency were thus achieved for DNA as well as for proteins from pathogens. This optimized functionalization methodology was applied to InP nanowires that due to their low surface recombination rates were used as new active transducers for biosensors. The developed devices provide ultrahigh label-free detection sensitivities ~1 fM for specific DNA sequences, measured via the net change in device electrical resistance. Similar levels of ultrasensitive detection of ~6 fM were achieved for a Chagas Disease protein marker (IBMP8-1). The developed InP nanowire biosensor provides thus a qualified tool for detection of the chronic infection stage of this disease, leading to improved diagnosis and control of spread. These methodological developments are expected to substantially enhance the chemical robustness, diagnostic reliability, detection sensitivity, and biomarker selectivity for current and future biosensing devices.

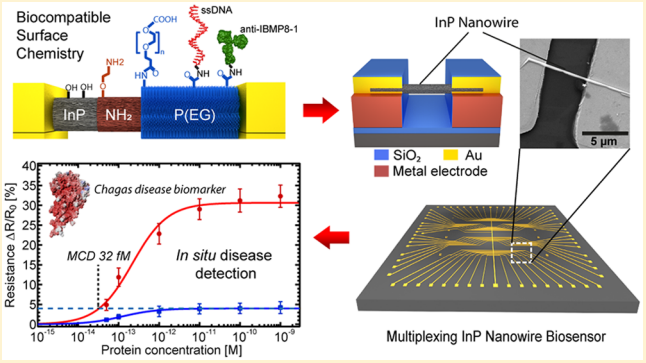

KEYWORDS: *Biosensor, nanowire, indium phosphide, Chagas Disease, field effect transistor, surface chemistry*

The efficient detection of exiguous fractions of specific biomolecules is a challenge in medical diagnostics and life science due to important applications in disease diagnosis, environmental monitoring, and drug discovery, among others.[1,2] The majority of the current detection methods rely on specific labeling techniques or on the binding of enzymatic ligands to a specific target molecule.[3−5] Both processes, however, require a large amount of target biomolecules for reliable detection, increasing diagnosis time and screening test expenses. These shortcomings have drawn the attention of the community to label-free, real-time monitoring electronic biochemical sensors during the past decade, based on one- and two-dimensional nanostructures. In particular, nanoscale biosensors based on field effect transistors (nano-FET) garnered substantial research effort owing to the capability of detecting extremely small amounts of biomolecules in physiological solution, thus providing an important tool for early disease detection and improved treatment. The majority

Received: April 29, 2017
Revised: August 25, 2017
Published: September 12, 2017

DOI: 10.1021/acs.nanolett.7b01803
Nano Lett. XXXX, XXX, XXX−XXX

of label-free nanoscale FET biosensors rely on changes in conductivity or impedance upon biomarker binding to its specific bioreceptor.[6,7] Furthermore, such FET configurations provide rapid electrical detection, multiplexing, portability, and system-on-a-chip device integration of both the sensing component and read-out system.

The employment of nanowires (NWs) as detection-efficient biosensors rely on the fact that they are more effective bioelectrochemical transducers, compared to their thin film analogs. This is due to their large surface-to-volume ratio and unidirectional conduction channels, which are very sensitive to minute surface perturbations during binding events.[6−9] Understanding signal transduction mechanisms and the impact of important device parameters is a necessary step to significantly improve the performance and reliability of such biosensor devices. Therefore, the effect of several parameters on FET sensitivity, such as dimensions,[10] material composition,[11] electrode material,[12] type of receptor molecule,[13] gate bias,[9,14] ion concentration,[15] and methods of analyte delivery,[16,17] have been reported. However, no detailed studies have investigated the applied surface functionalization composition and quality, which are crucial factors for the overall biosensing sensitivity and measurement reliability.

In fact, the chemical composition of the applied surface functionalization correlates with biosensing sensitivity via the density of specific bioreceptors provided. The majority of silicon nanowire-based developments consider, nowadays, the covalent binding of receptor molecules via silica monolith linker to surface oxides to provide an increased bioreceptor density, enhancing on that account the chemical stability and bioreceptor linkage lifetime in physiological solutions.[6,9,18−23] In an ideal design, the organochemical bioreceptor matrix should provide a well-organized monolayer surface coverage with high receptor density, stable chemical attachment, high biocompatibility, and suppression of nonspecific target biomolecule adhesion.[24−26] These two latter features are significant because nonspecific adhesion of biomarkers decrease subsequently the biosensor sensitivity and specificity for real-world applications. For bioreceptor attachment, alkoxysilanes have been the main choice as surface anchor despite nonhomogeneous coatings using wet chemistry.[27−30] As a result, the receptor density decreases, hampering the detection sensitivity. In contrast, the alternative approach using ethanolamine (EA) as surface linker provides highly reproducible homogeneous and dense monolayer-coatings that may be applicable for nanostructures.[31,32] Moreover, biocompatibility and nonspecific adhesion-suppressing capacity of biosensor coatings could be obtained using additionally physically and chemically inert poly(ethylene glycol) (PEG) cross-linkers.[32−35] The flexibility of PEG cross-linker and the increased distance to the surface they provide for the bioreceptor may further facilitate protein biomarker capture binding due to decreased steric hindering, rendering current complex processes for controlled antibody orientation attachment redundant.[36−38]

In addition to high quality functionalization processes, the performance of nanowire-based FET biosensors also depends on the choice of the conduction channel material. Silicon nanowires are prevalent among single crystalline materials, partly due to the facile synthesis capabilities.[39] On the III−V semiconductor material category, InAs nanowires exhibited high sensitivity[8] when incorporated as active materials in FET biosensors. However, large area biosensors based on InP thin films have achieved DNA detection limits as low as 1 pM, representing a substantial increase in sensitivity when compared to other similar, microscale FET-based semiconductor biosensors.[40] Despite the similar electronic structure, compared to their III−V material counterparts[41] InP exhibits lower surface recombination rates and consequently longer carrier lifetimes which certainly impact the biosensor performance. This behavior has also been observed for wurtzite InP nanowires,[42] providing a strong argument for applying them as biosensor conduction channels.

Here, we report the fabrication of highly sensitive InP nanowire biosensor devices as well as a quantitative evaluation of EA and PEG functionalization quality to further understand key parameters controlling biosensor sensitivity and selectivity. Using quantitative fluorescence microscopy, atomic force, and Kelvin probe force microscopy, we show that the surface functionalization strategy using EA and PEG enhances drastically the surface coating quality and biomolecule detection efficiency for DNA and protein complexes, providing thus a biocompatible surface with a highly suppressing character of nonspecific biomolecule adhesion. The performance of EA and PEG-functionalized InP NW biosensors was evaluated using 40 and 80 base pair single strand (ss) DNA oligomers to assess the potential of the present methodology for rapid and reliable detection. Our devices have reached DNA detection levels as low as ∼1 fM as lower detection limit (LOD) and ∼7 fM for the detection of specific sequences within time frames lower than 30 min. Challenging biosensor tests were then performed for biomarker detection of Chagas Disease (CD),[43] or American trypanosomiasis, a deadly infection caused by the protozoan parasite *Trypanosoma cruzi*. Although mild in acute stages, a chronic CD infection can persist unnoticed for decades in about 30% of the infected individuals, eventually leading to devastating complications to human health.[44] Furthermore, the increasing CD spread to nonendemic countries poses a worldwide challenge[45] due to the low effectiveness of existing treatments for chronic patients and lack of sensitive and accurate diagnostic tools.[44,43] Hence, highly sensitive biodetection techniques, particularly those portable to allow access to remote regions, would vastly improve CD diagnosis and its spread control. For those reasons, we have tested our developed InP-based NW biosensors with a specific antigen for CD. Our results show specific detection limits to *T. cruzi* recombinant protein concentrations down to ∼30 fM with an LOD of ∼6 fM within the same time frame of <30 min observed for specific DNA detection. Our device performance thus exceeds those based on two-dimensional (2D) materials like graphene and reduced graphene oxide,[46−49] MoS_2,[50,51] and even surpasses the performance of InAs and Si nanowire-based FET biosensors.[6,21−23]

Prior to the nanowire functionalization process, we first optimized and compared the surface coating efficiency and quality of both commonly used aminosilane (APTES)[18−20,27−30] and ethanolamine (EA) alternatives[31−34] as surface linkers to broad area borosilicate substrates (amorphous SiO_2), using the wet chemistry approach. We can, thus, compare directly the quality of coatings obtained without assessing the influence of curing temperatures and low pressures during the functionalization process to the nanostructures.[30] The coating quality evaluation was performed using quantitative widefield fluorescence microscopy (WFM) by coupling covalently carboxyl-modified Atto647N fluorophores to the accessible amino groups of both surface linkers (Figure 1A,B).[32]

DOI: 10.1021/acs.nanolett.7b01803
Nano Lett. XXXX, XXX, XXX−XXX

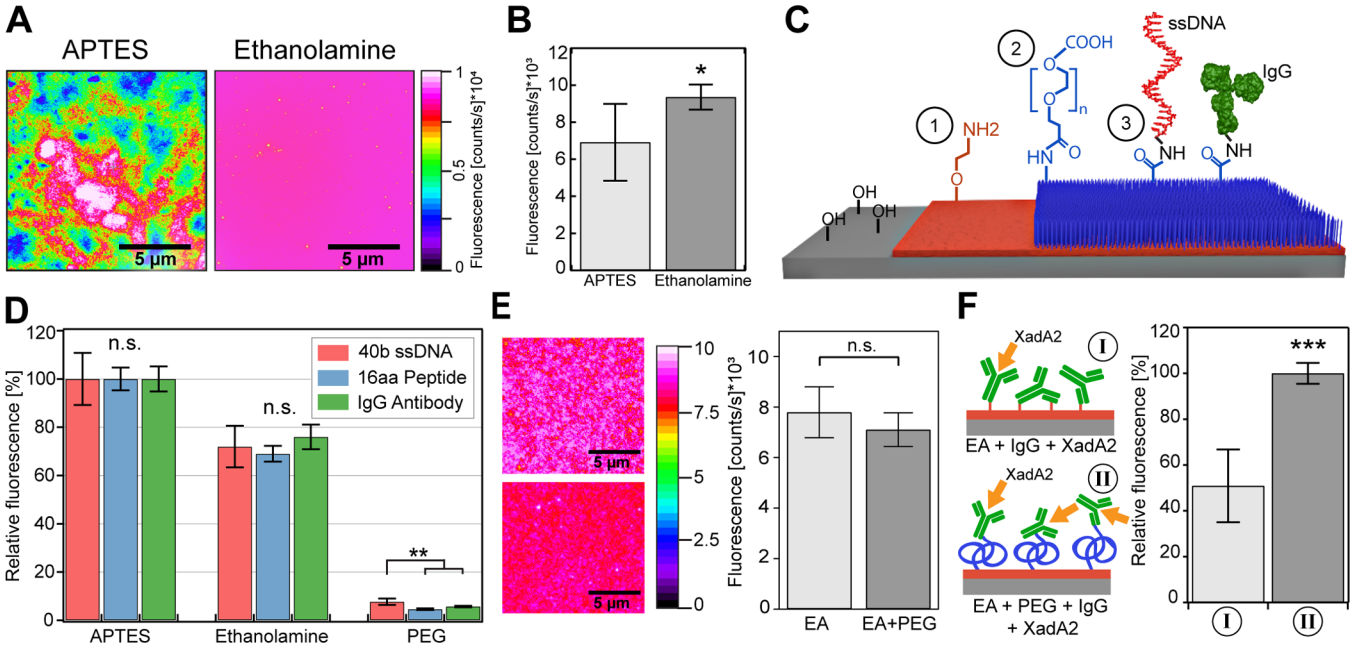

Figure 1. Surface functionalization with APTES, ethanolamine, and passivation using poly(ethylene glycol). False-colored widefield fluorescence images (A) depict the coating quality of APTES (n = 13) and EA (n = 14), visualized via covalent attached Atto647N fluorophores. Bar plot (B) exhibits the compared quantitative fluorescence mean density ($\bar{x} \pm \delta$) of both surface coatings. (C) Schematic representation of the functionalization procedure includes EA-coupling to surface hydroxyl-groups (1), the attachment of heterobifunctional PEG cross-linker (2), and subsequent covalent binding of biomolecules via peptide-binding (3). Comparison histogram illustrates average nonspecific adhesion ($\bar{x} \pm \delta$) of different fluorophore-labeled biomolecules (D) on different surface coatings, normalized to the quantities measured on APTES. (E) False-colored widefield images (left panel) of Alexa674-labeled antibodies covalently bound to EA and PEGylated surfaces, together with the bar plot (right panel, n = 10 each) presenting the corresponding quantitative fluorescence mean densities ($\bar{x} \pm \delta$). (F) Schematic illustration (left panel) of randomly oriented covalent antibody coupling to EA (I) and PEGylated (II) surfaces. The addition of a PEG cross-linker (n = 7 for each condition) increases strongly anti-Xf.XadA2/Xf.XadA2 antibody:protein binding efficiency ($\bar{x} \pm \delta$). The data shown in (B,D,E,F) were subject to statistical analysis using unpaired, two-tailed t-test with significance levels of α = 0.05 (*), α = 0.001 (**), and α = 0.00001 (***); n.s. = nonsignificant.

The APTES coating leads to undesirable inhomogeneous coverage (Figure 1A), in agreement with previous observations.[27−30] In contrast, the EA surface layer provides a homogeneous coverage. The quantitative analysis (Figure 1B) reveals a significantly higher average linker density (~37%) for EA compared to the APTES coating. Moreover, the surface linker density varies significantly more for APTES (σ = ~40%) than for EA-coated surfaces ($\sigma \leq$ 7%). Furthermore, the influence of added NHS-PEG-$COOH_{MW3400}$ cross-linker (Figure 1C) on the suppression character of nonspecific adhesion was examined via surface-adhesion experiments with different types of fluorophore-labeled biomolecules. In comparison to the standard approach using APTES, EA coating leads to equivalent adhesion reduction of ~30% in average (Figure 1D) for single-stranded 40b ssDNA (DNA sequences listed in Supporting Information Table S1), a 16 amino acid containing random peptide sequence, and the polyclonal Xf.XadA2 IgG antibody, an afimbrial adhesin of the bacteria *Xylella fastidiosa*.[40,52] The decrease in adhesion can be explained by the more homogeneous and dense surface coverage of the EA linker whereas the defective APTES coverage can expose bare SiO_2 areas where strong electrostatic biomolecule interaction can readily occur. The further addition of chemically and physically inert PEG-biomolecules significantly suppresses nonspecific adhesion, reducing the fraction of nonspecifically adhered biomolecules to ≤8% for all types of biomolecules tested. This observed surface passivation efficiency should provide a substantial improvement in the signal-to-noise ratio during biosensing and consequently increase the detection specificity.

We further questioned the degree of steric hindrance of large target biomolecules upon binding to their specific surface-attached bioreceptors depending on the distance to the substrate surface and their mobility in three dimensions. To evaluate the effect, we first assessed the covalent antibody binding density on EA-coated and PEGylated surfaces (Figure 1E). While the EA-coating shows higher variance in coating homogeneity and density compared to PEGylated surfaces, both coatings show statistically similar antibody densities. On the basis of previous observations describing that the spatial orientation of surface-immobilized antibodies impacts the antigen-binding performance, we investigated the effect of increased surface distance and spatial mobility on antigen binding via added PEG cross-linker.[36−38] To quantitatively evaluate the impact of PEG, we used the antigen/antibody complex from the afimbrial adhesin Xf.XadA2[40,52] for comparison. In our experiment, we covalently coupled polyclonal anti-Xf.XadA2 antibodies directly to both EA surface and PEG-coating (Figure 1F, left panel). The amount of specifically bound Xf.XadA2 ligand protein surprisingly increases 2-fold (Figure 1F, right panel) with the addition of a PEG cross-linker. The flexible PEG cross-linker provides a larger distance to the substrate surface, increased spatial mobility in three dimensions, increased distance between individual antibodies, and decreased amount of multiple chemical bonding. These circumstances allow a higher degree of freedom in the orientation of the antibodies, and steric

DOI: 10.1021/acs.nanolett.7b01803
Nano Lett. XXXX, XXX, XXX−XXX

hindrance of antigen binding is thus reduced. Antibody orientation and steric hindrance of antigen binding were previously identified as parameters of highest impact, leading to antibody immobilization strategies that require a more complex functionalization methodology, involving localized antibody labeling or proteins and aptamers that bind specifically to the Fc region of the antibody for orientation-controlled immobilization.[36−38] On the basis of our observations, the use of PEG cross-linker renders such specific binding methodology redundant with the additional benefits of exploiting the biocompatibility and unspecific-adhesion suppressing character of PEG.

The Xf.XadA2-functionalized surface and PEG monolayers were measured using atomic force microscopy (AFM) and WFM (Figure 2). To verify the presence of surface-

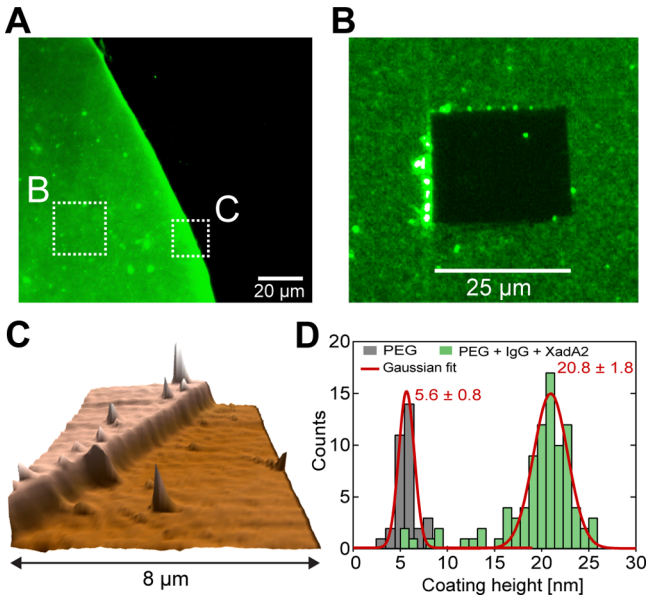

Figure 2. Fluorescence images and AFM topography of protein-functionalized surfaces. Simultaneous AFM and widefield fluorescence microscopy (A) was applied to covalently bound Xf.XadA2 proteins on PEGylated substrates, visualized via Alexa488-labeled secondary antibody. The Xf.XadA2-coated surface was scratched (B) using high forces ≥2 nN in rectangular shape (region B). At the edge of the Xf.XadA2 functionalized area (region C), AFM topography measurements (C,D) demonstrate the successful functionalization by the elevated plateau of the coating. The histogram (D) exhibits the coating heights measured for the PEG coating (gray) and Xf-XadA2-functionalized surface, including Alexa488-labeled secondary antibodies.

immobilized Xf.XadA2, the coated surface was scratched at high forces (≥2 nN, Figure 2B) with the AFM cantilever, while the WFM signal of Alexa488-labeled antibody was used to track visually the scratching of the functionalized surface. The coating heights of both the PEG-layer and the Xf.XadA2-coated surface were investigated via AFM topography measurements (Figure 2C,D) at the coating edges. The PEG coating (Figure 2D, gray bars) shows an average height of 5.6 ± 0.8 nm, in close agreement with the Flory radius estimation of PEG polymers with a molecular weight of 3.4 kDa.[53] The Xf.XadA2-coated surface (Figure 2C, green bars) exhibits in average a height of 20.8 ± 1.8 nm, adding as such ∼15 ± 3.5 nm to the PEG-layer. Depending on the spatial orientation of the IgG antibodies to the surface, and the linker stiffness, the encountered height can cover a range between 5 to 15 nm.[54] Because of the flexible PEG cross-linker used for protein anchorage, the Xf.XadA2 proteins and their antibodies form a layer with random orientation. In this scenario, we would expect an average height of ∼10 nm for the antibodies, similar to IgG monolayer thicknesses reported previously.[54−56] The mass of Xf.XadA2 protein is with ∼20 kDa comparable to the size of the antibody's single chain variable fragment, adding ∼3−4 nm to the total height.[57] Taken together, the measured total height of the antibody/antigen layer with ∼15 ± 3.5 nm is compatible with the expected protein dimensions.

Prior to functionalizing InP nanowires, the transferability of the surface functionalization methodology to InP thin film substrates was examined by comparing the coating homogeneity and DNA immobilization density (Figure 3A). SiO_2 and InP thin film supports were functionalized with EA and PEG with the same protocol, and 40b probe ssDNA was covalently immobilized to the PEG layer. The hybridization of complementary, Atto647N-labeled 40b target ssDNA allowed the comparison of both the surface homogeneity (Figure 3A, left panel) and DNA density (Figure 3A, right panel) on both materials. Despite the observed average DNA density being ∼5% lower for InP surfaces in comparison to SiO_2, the coating homogeneity and DNA densities are statistically comparable. This result attests the transferability of the surface functionalization methodology to InP, keeping characteristics previously observed for SiO_2.

In order to further evaluate the nature of the different surface coatings and their surface charge distribution, we performed Kelvin probe force microscopy (KPFM) measurements on broad area InP thin film surfaces where 80b ssDNA were immobilized covalently on PEGylated substrates (Figure 3B,C). This DNA sequence (Supporting Information Table S1) is also used for the *in situ* biosensor experiments.

In these measurements, the topography and surface potential (SP) of the functionalized surfaces were acquired simultaneously. Figure 3B,C shows the surface potential distribution for InP thin film surfaces functionalized with 80b probe DNA and 10 μM of complementary 80b target DNA hybridized to it, respectively (associated topography data are shown in Supporting Information Figure S1). A more uniform coverage is observed for probe-DNA; the larger SP variation observed for target-DNA indicates that hybridization occurs nonhomogeneously with low coverage density as compared to probe DNA on the surface. A single strand of DNA chain is basically negatively charged owing to the presence of phosphate groups in the backbone. Upon hybridization, the negative net charge increases, and thus the observed increase in negative SP values and SP variation across the surface. These variations, however, are not correlated to the observed surface RMS (average, root mean squared) roughness (Figure 3D). No significant differences in the RMS roughness values of DNA-functionalized surfaces were observed, even for hybridized target-DNA at rather different concentrations (Supporting Information Figure S1). However, RMS roughness increased significantly for PEG-functionalized InP surfaces when compared to both the pristine InP thin film and DNA-covered surfaces, as expected for a porous polymer.[35]

Ideally, complementary ssDNA should only attach to its specific probe-DNA, providing no net change in the surface topography. Hence, no change in RMS values are expected, as indeed observed. On the other hand, SP values show unique characteristics of the surface-tethered biomolecules (Figure

DOI: 10.1021/acs.nanolett.7b01803
Nano Lett. XXXX, XXX, XXX−XXX

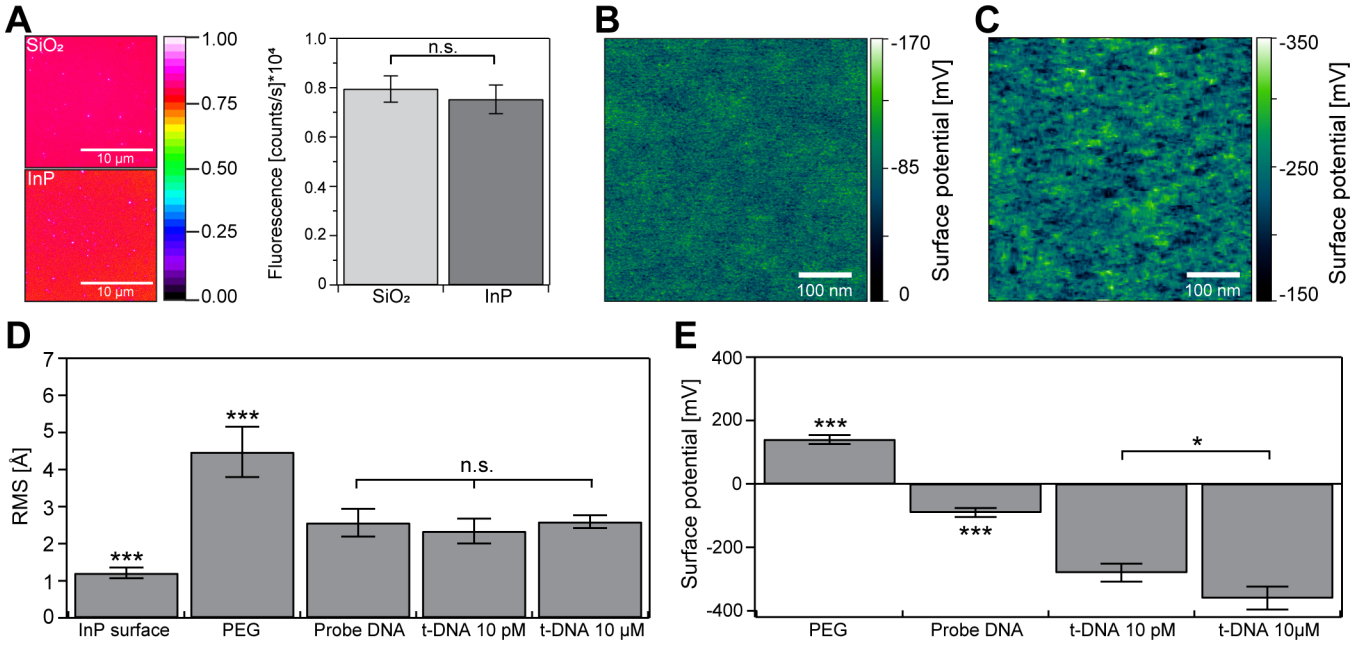

Figure 3. Surface functionalization, roughness, and surface potential of different surface coatings on InP thin film. (A) EA and PEG surface functionalization and covalent 40b DNA immobilization on SiO_2 and InP surfaces. The false-colored widefield fluorescence images (left panel) show the quality of DNA surface coating visualized via hybridized, Atto647N-labeled 40b target DNA. The bar plot (right panel) depicts the quantitative fluorescence mean density ($\bar{x} \pm \delta$; n = 18 each) for DNA coatings on both surface materials. (B,C) Kelvin probe force microscopy images show the surface potential of samples coated with 80b probe-DNA (B) and 10 μM of hybridized complementary 80b target DNA (C). The bar plots show the surface roughness (D) and surface potential (E) of the different surface coatings in comparison. The error bars on the bar plots denote the mean standard deviation ($\pm\delta$) and the shown data in (A,D,E) were subject to statistical analyses using unpaired, two-tailed t-test with significance levels of α = 0.05 (*), and α = 0.00001 (***); n.s. = nonsignificant.

3E). A net increase (decrease) in SP value is detected upon PEG (DNA) functionalization. Moreover, a systematic decrease in the SP values correlates with increased concentrations of target DNA upon hybridization. However, SP values of dry functionalized samples, as those used for KPFM measurements, cannot be taken as an absolute reference of DNA surface concentration. A 2-fold increase in RMS values as well as a 50% increase in the average SP variation occur upon increasing the N_2 purge time in the AFM chamber from 30 to 60 min (Supporting Information Figure S2). This result indicates a highly hydrated coating layer,[58,59] and the local reconfiguration of the tethered biomolecules upon water removal. Therefore, KPFM provides mainly a qualitative tool for surface coating evaluation; in a few cases when this layer shows larger height variations, corresponding to a more inhomogeneous topography, larger and discrete SP domains are observed. Large area biosensors fabricated from such surfaces show roughly no detection sensitivity to the specific biomolecule. Comparatively, the homogeneous SP image shown in Figure 3B,C indicates that any spatial domains for biomolecule immobilization are below the lateral resolution of the KPFM technique.

The characterization of the functionalization for broad area borosilicate glass and InP substrates discussed above provide concrete evidence of the successful covalent coupling of different bioreceptor (probe) molecules that allow the capture of specific target molecules. For the realization of an InP nanowire-based biosensor, we thus applied this same functionalization methodology to n-doped InP semiconductor nanowires that were grown using gold nanoparticles as catalysts, as described elsewhere.[60] The tapered InP nanowires can be grown up to 30 μm in length and 50−100 nm in average diameter in wurtzite crystalline phase (Figure 4A). For device purposes, these nanowires were mechanically removed from the as-grown GaAs substrates and dispersed in polar aprotic dimethyl sulfoxide (DMSO) solvent. InP nanowires were then initially functionalized with EA, afterward PEGylated and subsequently covalently functionalized with 40 b amino-labeled probe ssDNA (Figure 4C). The evaluation of DNA-nanowire functionalization was performed using Atto647N-labeled 40 b complementary target ssDNA (Supporting Information Table S1). The spectral analysis of the intrinsic photoluminescence (PL) of the InP material (Figure 4B, black line) exhibits PL-emission at 850 ± 50 nm, in agreement to previous reports.[61,62] Using confocal laser scanning microscopy (CLSM) to improve spatial resolution, we observe inhomogeneous PL-intensities along the nanowires (Figure 4C, lower CLSM panel), which were only functionalized with nonfluorescent 40 b probe ssDNA. The observed inhomogeneity in PL intensity along InP nanowires is mainly attributed to variations in trap state density and its effect on local excitonic properties.[61,62] However, upon binding of complementary Atto647N-labeled 40 b target ssDNA, the luminescence emission shows an overall 2-fold increase in intensity and remains fairly constant along the InP nanowire length (Figure 4D). This observation is consistent with the drop in the average SP values for complementary target DNA as compared to probe DNA (Figure 3B,C,E), both results indicating that hybridization actually occurs. The complementary spectral analysis of these DNA-functionalized InP nanowires (Figure 4B, red line) identifies both the characteristic emission spectra of the Att647N fluorophore between 660−760 nm and the PL spectra of InP (Figure 4B, black line). Both results confirm the successful surface functionalization methodology and covalent ssDNA coupling to InP nanowires.

DOI: 10.1021/acs.nanolett.7b01803
Nano Lett. XXXX, XXX, XXX−XXX

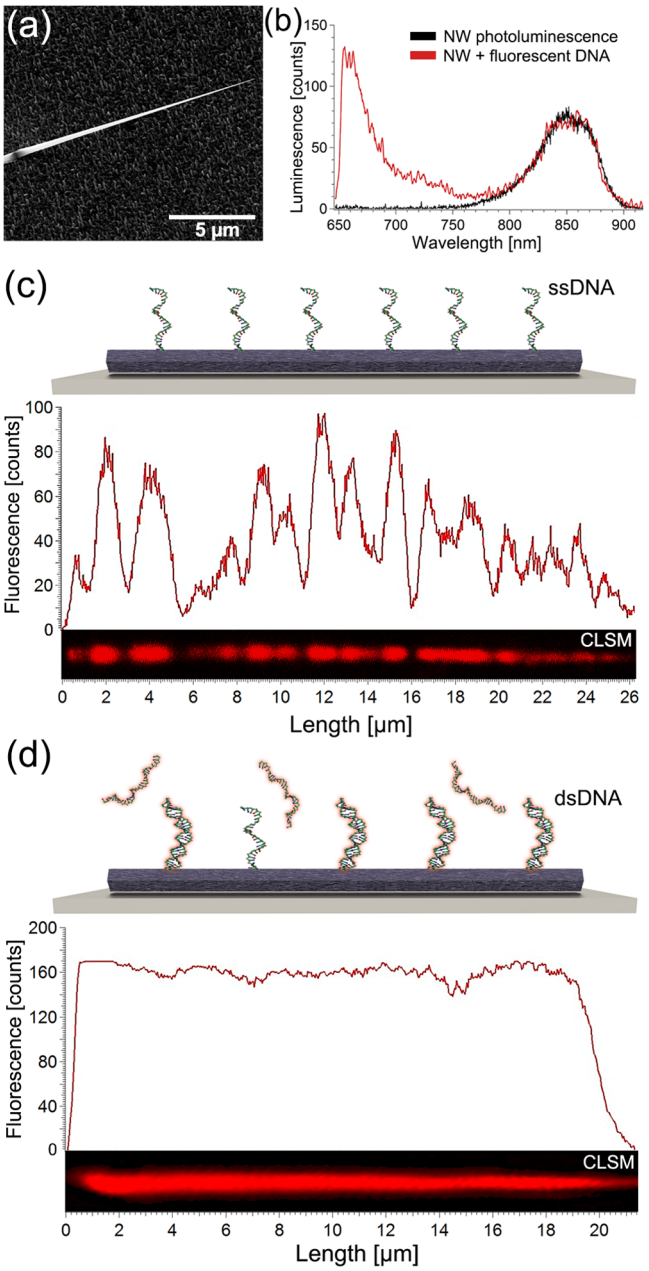

Figure 4. Functionalization of InP nanowires. Scanning electron microscopy image of as-grown InP NW sample (A). Spectral luminescence (B) shows PL signal of an InP NW (black line), superimposed with the emission of Atto647N-labeled 40b target ssDNA, and hybridized to a complementary ssDNA-functionalized NW (red line). CLSM images and fluorescence emission intensities along an individual InP NW (C) solely functionalized with 40b probe ssDNA and with hybridized Atto647N-labeled complementary 40b target ssDNA strand (D) verifying successful DNA functionalization.

The configuration used for our nanowire biosensor design consists of two terminals (representing source and drain), as shown in Figure 5A. A metal electrode based on Ni/Ge/Au alloy was used in order to keep the Schottky barrier with the n-doped InP nanowire as low as possible. The device fabrication process with nanowire alignment via microfluidic channels over arrays of electrodes is depicted in Figure 5B (see also Supporting Information Figure S3 and Materials and Methods). Polydimethylsiloxane (PDMS) based microfluidic channels with a width of 100 and 50 μm in height were used to flow solution containing suspended InP nanowires in isopropanol over the Au electrodes, at low flow speeds. The density of nanowires on the electrode pair can be tuned (Figure 5C,D) by controlling the flow rate. Each chip contains 4 different channels and 16 individual electrodes per channel (Supporting Information Figure S3). The effective sensing region of each nanowire is dictated by the gap of ~5 μm between the electrode pair (Figure 5C). An additional UV-photolithography step was employed in order to passivate the remaining part of the chip by depositing 30 nm thick SiNx layer outside the active parts of the sensor chip and metal pads (Supporting Information Figure S3). The InP nanowire electrodes were unaffected by any possible contamination during the fabrication process which has been confirmed by the mapping of important elements by field emission scanning electron microscopy (FESEM) and energy dispersive X-ray spectroscopy (EDS) techniques. Figure 5D shows the EDS mapping of the distribution of In, Au, and Si elements at a particular region of a nanowire crossing the gap between electrodes. The chip containing arrays of electrodes was processed further via rapid thermal annealing at 430 °C for 3 min in N_2 ambient for ohmic contact formation. Typical $I-V$ characteristics of pristine and annealed nanowire electrodes are shown in Figure 5E, which clearly indicates that rapid thermal annealing is necessary to reduce the ohmic resistance at the Au−InP interface. Typically, resistance values of a nonannealed, single InP NW are found in the range of few MΩ (Figure 5E).

The biosensing efficiency of the InP NW sensor was investigated by considering two different target biomolecules of interest: DNA and CD protein biomarker. In the former case, which serves as a standard for detection performance comparison for our biosensor, 80 b NH_2-labeled probe ssDNA molecules were used to selectively detect a complementary 80 b target DNA sequence with high degree of specificity (Supporting Information Table S1). The DNA was designed using a random sequence with a relative high G/C-content of 62.5%, lying still in the range encountered in exons of mammalian genomes.[63,64] The chosen G/C content (Figure S4A) provides a high thermodynamic stability (ΔG = −141 kcal/mol), minimizing the probability of breathing and secondary structure formation, such as hairpins and internal loops, which could intrinsically influence the biosensor response. The melting temperatures at the different concentrations (10 fM up to 1 nM) used during the *in situ* biosensor titration experiments do not fall below ~80 °C (Figure S4B,C), minimizing as such the DNA double-helix structure suffering from breathing at biosensor measurement temperatures of ~24 °C. The protein sensing capability was assessed using IBMP 8-1, a specific marker for positive CD immunodiagnostic in human serum.[65] In this latter case, anti-IBMP 8-1 IgG antibodies were tethered covalently to the PEG-functionalized nanowires in our device.

The typical $I-V$ characteristics of the different concentrations (10 fM up to 1 nM) of complementary 80 b target DNA, evaluated after 60 min of hybridization, are shown in Figure 6A. The $I-V$ characteristics curves show concentration-dependent linear behavior. On the other hand, nonspecific 80 b probe DNA does not show any significant variation in the $I-V$ characteristics (Supporting Information Figure S4A). Initially, the time period for DNA hybridization was evaluated by measuring the relative change in the resistance of the probe DNA functionalized nanowire electrode in the presence of 1 pM and 10 fM of complementary target DNA, and 1 pM of

DOI: 10.1021/acs.nanolett.7b01803
Nano Lett. XXXX, XXX, XXX−XXX

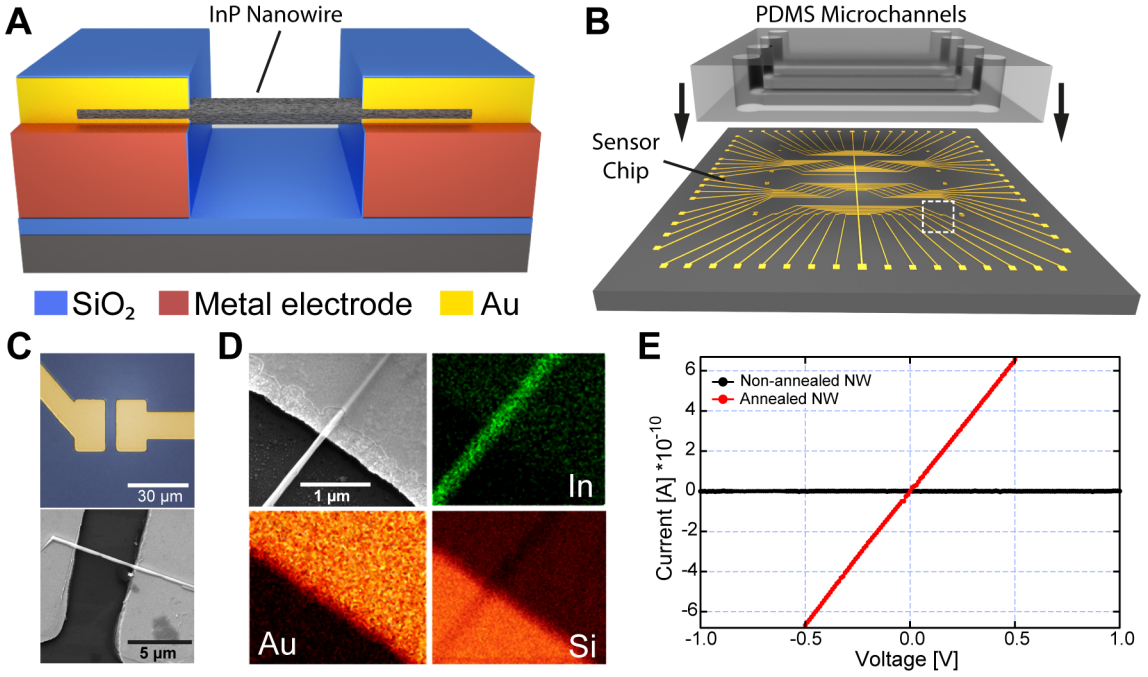

Figure 5. InP nanowire-based biosensor device. (A) Schematic representation of cross-sectional single InP NW configuration on SiO_2 substrate on metal alloys of Ti/Ni/Ge/Au and covered with an Au layer. (B) Schematic illustration of PDMS microfluidic device coupled to a sensor chip constituting of four individual channels, each channel covers 16 electrodes of the sensor chip. (C) Optical microscope image (top) of a single electrode pair with ~5 μm spacing in between, and FESEM image (bottom) of an electrode pair with an aligned single InP nanowire. (D) EDS elemental mapping images of different components after metallization process and RIE etching of a region of interest with attached nanowire. (E) Sensor device $I-V$ characteristics before and after the nanowire annealing process demonstrating the ohmic character of nanowire-electrode (InP–Au) contact.

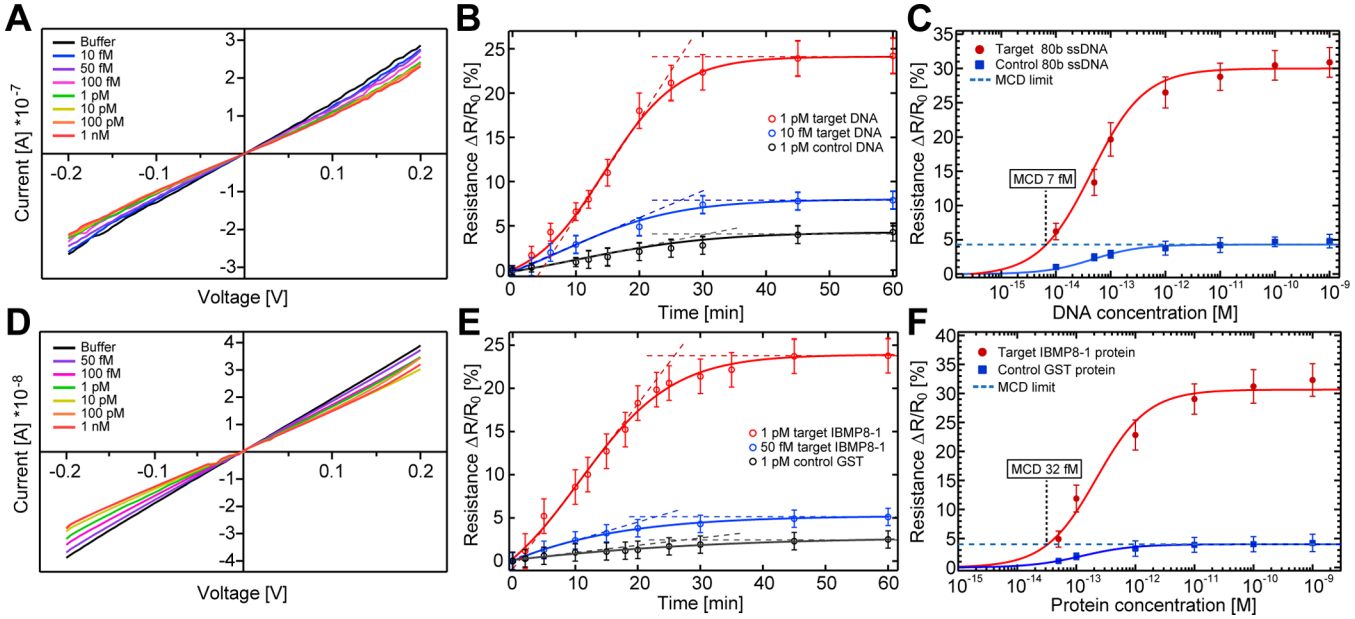

Figure 6. Electrical biosensor measurement with titration of 80 b ssDNA and *T. cruzi* IBMP8-1 antigen. Electrical biosensor $I-V$ response curves upon titration of (A) complementary target DNA and (D) specific *T. cruzi* target protein IBMP8-1. Resistance changes of the biosensor obtained upon titration of (B) complementary target DNA (red) and noncomplementary probe DNA (blue) (n = 4 each), and (E) specific *T. cruzi* recombinant antigen IBMP8-1 (red) or nonspecific Glutathione S-transferase (GST; n = 4 each) target (blue). (C,F) The resulting titration data are fitted to a Langmuir adsorption isotherm (lines) to characterize the biosensor performance. The MCD limits are shown for both biomolecular systems tested. For high and low concentrations of (C) DNA and (F) protein molecules, the biosensor saturation response is shown (B,E) over time until signal stabilization to estimate the signal equilibration times. The data are represented with the mean standard deviation error $\pm$ σ. The biosensor performance results for each tested biomolecular system are summarized in Table 1.

nonspecific DNA (control), as shown in Figure 6B. The results indicate that a time period of <30 min (x = 28 $\pm$ 2 min; n = 4) is sufficient to measure the hybridization to full extent via the substantial change in the nanowire resistance values until signal

DOI: 10.1021/acs.nanolett.7b01803
Nano Lett. XXXX, XXX, XXX−XXX

saturation for both target DNA and nonspecific DNA. Comparable $I-V$ characteristics (Figure 6D) and saturation curves (Figure 6E) were also obtained for the protein interaction assay, which was performed with the IBMP8-1 protein, which specifically binds to the immobilized polyclonal antibody, and with an unrelated protein (GST; glutathione S-transferase) as control (Supporting Information Figure S4B). The $I-V$ behaviors for both DNA and IBMP8-1 protein show that there is a significant change in the electrical properties of the InP nanowire sensor electrode upon specific target biomolecule attachment, which forms the basis of the presented device. It is also important to notice that the calculated Debye length for the physiological buffer conditions used for device sensing is around 1 nm, thus reliable detection would hardly take place using the 5 nm thick PEG surface layer (Figure 2D).[66] A possible explanation relates to the presence of the PEG layer on the surface; previous works have shown that dielectric properties in aqueous solutions can be altered by polymers.[67] More recently, PEG-functionalization of Si nanowire FET biosensors has been shown to indeed increase the effective screening length in the region immediately adjacent to the device surface.[68]

The relative resistance variation measurements of specific capture of target DNA and IBMP8-1 protein at different concentrations are shown in Figure 6C,F, respectively, representing the specific receptor/ligand interaction (Figure 6C,F; red lines) in comparison to the unspecific receptor:ligand controls (Figure 6C,F; blue line). Here, the combined change in electrical resistance ($\Delta R/R_0$) of all experimental repetitions showed no significant detection differences. The concentration titration for both specific receptor/ligand systems shows a clear increase of the biosensor resistance resulting in maximum variation values about 36% for probe DNA/target DNA and ~37% for anti-IBMP8-1/IBMP8-1, whereas the unspecific receptor/ligand measurements show nonspecific adsorbed DNA/protein and noncorrelated resistance variations with the concentration up to approximately 5% at highest concentration (1 nM) for both biomolecular systems. The specific interaction measurements follow a saturation behavior for both systems, which can be fitted by Langmuir adsorption isotherms (Figure 6C,F; Figure S6; Supporting Information methods) to gain information about the biosensor sensitivity.[49,68−70] The values obtained for the nonspecific biomolecule titration measurements render the minimal specific detection concentration (MCD), resulting in 7 fM for complementary ssDNA and 32 fM for the IBMP8-1 protein. While such MCDs reflect the lower concentration limits that can be measured with acceptable precision, accuracy and biomarker selectivity, they do not describe the lowest possible concentration detection limit of the analytes. From the analytical noise of the NW biosensor we can calculate with a confidence interval of 99.7% the limit of detection (LOD; Supporting Information methods) for each biomolecule system.[71] The LOD provides the possibility to compare the biosensor performance with previously reported developments, as the majority of the conducted studies lack adhesion-suppressing coatings or do not consider the fraction of nonspecifically adhered biomolecules. The titration results for each biomolecular system obtained in this study using the presented InP NW devices are summarized in Table 1. The reported MCD and LOD results are quite remarkable considering the simplicity of the InP nanowire device for biosensing tests, working with no field effect amplification and average nanowire diameters larger than

Table 1. Biosensor Titration Results for Each Biomolecular System[a]

	LOD	MCD	LSR	SSR	EqT [min]
80 bp DNA	1.4 fM	7 fM	15−130 fM	>480 fM	28 ± 2
IBMP8-1 protein	5.7 fM	32 fM	90−500 fM	>950 fM	26 ± 3

[a]Concentration limit of detection (LOD), minimal concentration detection (MCD), defined sensitivity regions (LSR, linear sensitivity region; SSR, sensor saturation region), and biosensor equilibrium time (EqT) for specific DNA and IBMP 8-1 detection. The values were obtained from $n = 4$ nanowires for each biomolecular system tested.

surface depleted regions.[72] Moreover, despite the good receptor uniformity and capture binding performance exhibited by our functionalization protocol, no further receptor density optimization was performed prior to the biosensing tests.

When compared to similar devices in literature, the obtained detection limits of our InP nanowire biosensor development (LOD: protein 5.7 fM/DNA 1.4 fM) surpass the detection sensitivity over several magnitudes of previous protein and DNA biosensor key studies using graphene,[46,47] reduced graphene oxide[48,49] and 2D transition metal chalcogenides ($MoSe_2$)[50,51] in the FET configuration (see biosensor detection limit comparison in Supporting Information Table S2). When compared to InAs nanowire devices with a protein detection limit of 10 pM (Avidin),[8] our InP nanowire sensor shows far superior sensing performance. Furthermore, when compared to silicon nanowire based biosensors (MCD protein, 200 pM/LOD DNA, 60 fM),[6,23] the presented biosensor shows especially for protein biomarker detection a strong increase in sensitivity, most likely due to the applied cross-linker and improved linker coverage, as described in the previous sections. In this context, we note that the comparison to other nanowire biosensors is performed with respect to the same device configuration without the usage of an additional back-gate; nanowire device sensitivity can be enhanced by operation in the subthreshold regime where the gating effect of molecules bound on a surface can be increased due to the reduced screening of carriers in nanowires.[9,14] This methodology allowed an additional increase of detection sensitivity (LODs: protein 2 fM/DNA 0.1 fM)[9,21,22] which are closer to the performance we achieved in our device without gate-based capacitance attenuation. We thus expect that this methodology would further improve the sensitivity of the presented InP NW biosensor development.

With regard to CD diagnosis, commonly used methods, such as enzyme-linked immuno sorbent assay (ELISA) and polymerase chain reaction (PCR), achieve sensitivities in the nanomolar range (LODs: ELISA ~30 nM; PCR ~10 nM),[73−75] close to two-dimensional electrochemical immunosensors with LODs ~1−2 nM.[73,76] More recent electrochemical immunosensors with nanoscale gold particles as transducers are able to detect target CD proteins with an LOD ~20 pM.[77] In comparison, the presented InP NW biosensor surpasses the detection limit of the existing diagnosis methods ~1000-fold, which may allow the detection of chronical Chagas infection more reliably, overcoming the limitation of the antibody titer in the human blood serum, which is usually very low in such cases.[44,45] Since IBMP8-1 is a chimeric *T. cruzi* protein developed for diagnostic purposes using ELISA assays, we have carried out surface plasmon resonance (SPR) measurements to compare biosensor antigen/antibody interaction sensing capabilities (Figure S6, Table S3).[65] A similar protocol

DOI: 10.1021/acs.nanolett.7b01803
Nano Lett. XXXX, XXX, XXX−XXX

was followed to immobilize the antibodies on the SPR Au substrate; however, no PEG-linker was used in this case in order to enhance SPR sensitivity.[78] As expected, SPR measurements provided reliable detection only at much higher protein concentrations with an LOD of ~2 nM (Table S3) than the InP NW biosensor. Signal saturation is achieved within similar timeframes (≤30 min) for both biosensors. On the other hand, binding kinetics measurements with FET sensors are still subject of recent developments in literature.[79,80] The kinetics data obtained from the InP NW biosensor shows a notable difference (Table S3) from the SPR technique, which is more widely accepted for this type of measurement. The discrepancy could arise, for example, if the functionalization protocol does not provide proper receptor densities,[79] despite the homogeneous antibody coverage indicated by our extensive functionalization characterization on SiO_2 and InP surfaces. However, the presence of the PEG-linker in the InP nanowire biosensor can account for improved ratios of protein capture and specific/nonspecific binding rates which provide a much lower background biological noise floor for enhanced detection sensitivity.[81] Further studies are necessary to investigate this point, which could be targeted using an optimized FET version of our InP nanowire device.

Our study demonstrates the successful functionalization of inorganic InP nanostructures with ssDNA and protein biomolecules using a simple yet powerful functionalization methodology. Our in-depth characterization of the functionalization show significant improvement in bioreceptor density and coating homogeneity by applying EA in comparison to alkoxysilanes (APTES) using simple wet chemistry processes. Furthermore, by adding biocompatible PEG cross-linkers the methodology leads to (i) significantly higher ligand binding specificity due to its efficient nonspecific adhesion suppressing capacity; (ii) increased receptor/ligand binding based on spatial separation between the bioreceptors and to the surface; (iii) additional degrees of freedom and spatial mobility for immobilized antibodies, leading to decreased steric hindrance for antigen binding; and (iv) minimized Debye screening for biosensing applications. We also demonstrate that label-free biosensors based on InP nanowire transducers can achieve ultrahigh-sensitivity for ssDNA over a wide linear operation range (fM to pM) with high degree of selectivity. Furthermore, we show that the developed biosensor is also highly sensitive in detecting very low concentration of CD biomarker, IBMP8-1. The high sensitivity biomarker detection, using nonpurified antibodies from serum, creates a reliable alternative for diagnosing chronic infections which exhibit very low antibody levels in the host. In addition, this development provides the potential to significantly enhance the chemical robustness, detection reliability and, most importantly, the overall detection sensitivity and biomarker selectivity for current and future label-free nanoscale biosensors.

Materials and Methods. Materials and experimental details of material syntheses, surface functionalization, microscopy, surface plasmon resonance, and device fabrication techniques are described in detail in the accompanied Supporting Information.

■ ASSOCIATED CONTENT

Supporting Information

The Supporting Information is available free of charge on the ACS Publications website at DOI: 10.1021/acs.nanolett.7b01803.

Detailed methodological description of material syntheses, surface functionalization, microscopy, surface plasmon resonance measurements, biosensor device fabrication, and supporting figures and tables (PDF)

■ AUTHOR INFORMATION

Corresponding Authors

*E-mail: r.janissen@tudelft.nl. Phone: +31-15-2783552.
*E-mail: monica@ifi.unicamp.br. Phone: +55-19-35215338. Fax: +55-19-35215376.

ORCID

Monica A. Cotta: 0000-0002-2779-5179

Present Addresses

(P.K.S.) Department of Physics, University of South Florida, Tampa, FL 33620-7100.
(D.B.A.) Department of Physics, University of Michigan, Ann Arbor, MI 48109-1040

Author Contributions

R.J. and P.K.S. contributed equally. P.K.S. carried out microfluidics fabrication and biosensor assembly, FESEM and EDS measurements and biomarker titration experiments. R.J. contributed with surface functionalization experiments, combined AFM fluorescence and WFM imaging, data analysis, and assembling the plots and figures. C.A.S. expressed and purified the Xf.XadA2 proteins, under A.P.d.S. supervision. A.M.d.S. contributed with DNA functionalization and Kelvin probe force microscopy measurements. R.J. and D.B.A. obtained the spectroscopic luminescence data. A.A.v.Z. developed metallization protocols and device processing. A.D.T.C., P.C., and N.I.T.Z. provided biological material and input on CD diagnostics. D.S.O. performed InP nanowire growth. D.E.P.S. and L.T.K. contributed with SPR measurements and biosensing discussions. C.L.C. discussed the setup for spectroscopy experiments. R.J., P.K.S., and M.A.C. designed the study and wrote the article. M.A.C. supervised and managed the whole study. The manuscript was written through contributions of all authors. All authors have given approval to the final version of the manuscript.

Funding

This work was supported by the Brazilian funding agencies FAPESP (2015/16611-4, 2013/02300-1, 2010/51748-7), CNPq (479486/2012-3, 404242/2012-0, and 590032/2011-9) and CAPES.

Notes

The authors declare no competing financial interest.

■ ACKNOWLEDGMENTS

R.J., P.K.S. and D.S.O. acknowledge scholarships from FAPESP and A.M.S. and D.B.A. from CAPES/CNPq. Access to confocal microscopy was granted by INFABIC/UNICAMP (FAPESP 08/57906-3, CNPq 573913/2008-0). We acknowledge access to electron microscopy (LME) and microfabrication (LMF) facilities at the National Nanotechnology Laboratory (LNNano, Brazil) and clean room facilities at both Semiconductor Component Center (CCSNano, UNICAMP) and Device Research Laboratory (IFGW, UNICAMP). Xf.XadA2 antibodies were provided by Dr. A. A. de Souza (IAC, Cordeirópolis, São Paulo, Brazil). The authors are greatly indebted to A. Gobbi and M.H. Piazzetta from LMF/LNNano for PDMS microfluidics processing, Dr. A. Kisner from IQ/UNICAMP

DOI: 10.1021/acs.nanolett.7b01803
Nano Lett. XXXX, XXX, XXX−XXX

and P .C. Galvão, from IQ/UNESP, for technical assistance during this work.

REFERENCES

(1) Giljohann, D. A.; Mirkin, C. A. Drivers of Biodiagnostic Development. *Nature* **2009**, *462*, 461−464.
(2) Turner, A. P. F. Biosensors: Sense and Sensibility. *Chem. Soc. Rev.* **2013**, *42*, 3184−3196.
(3) Lequin, R. M. Enzyme Immunoassay EIA./enzyme-Linked Immunosorbent Assay ELISA. *Clin. Chem.* **2005**, *51*, 2415−2418.
(4) Heller, M. J. DNA Microarray Technology: Devices, Systems, and Applications. *Annu. Rev. Biomed. Eng.* **2002**, *4*, 129−153.
(5) Khoodoo, M. H. R.; Sahin, F.; Donmez, M. F.; Jaufeerally Fakim, Y. Molecular Characterisation of Xanthomonas Strains Isolated from Aroids in Mauritius. *Syst. Appl. Microbiol.* **2005**, *28*, 366−380.
(6) Maedler, C.; Kim, D.; Spanjaard, R. A.; Hong, M.; et al. Sensing of the Melanoma Biomarker TROY Using Silicon Nanowire Field-Effect Transistors. *ACS Sensors* **2016**, *1*, 696−701.
(7) Patolsky, F.; Zheng, G.; Lieber, C. M. Nanowire-Based Biosensors - Analytical Chemistry ACS Publications. *Anal. Chem.* **2006**, *78*, 4260−4269.
(8) Upadhyay, S.; Frederiksen, R.; Lloret, N.; De Vico, L.; Krogstrup, P.; Jensen, J. H.; Martinez, K. L.; Nygard, J. Indium Arsenide Nanowire Field-Effect Transistors for pH and Biological Sensing. *Appl. Phys. Lett.* **2014**, *104*, 203504.
(9) Gao, X. P. A.; Zheng, G.; Lieber, C. M. Subthreshold Regime Has the Optimal Sensitivity for Nanowire FET Biosensors. *Nano Lett.* **2010**, *10*, 547−552.
(10) Li, J.; Zhang, Y.; To, S.; You, L.; Sun, Y. Effect of Nanowire Number, Diameter, and Doping Density on Nano-FET Biosensor Sensitivity. *ACS Nano* **2011**, *5*, 6661−6668.
(11) Li, C.; Curreli, M.; Lin, H.; Lei, B.; Ishikawa, F. N.; Datar, R.; Cote, R. J.; Thompson, M. E.; Zhou, C. Complementary Detection of Prostate-Specific Antigen Using In2O3 Nanowires and Carbon Nanotubes. *J. Am. Chem. Soc.* **2005**, *127*, 12484−12485.
(12) Minot, E. D.; Janssens, A. M.; Heller, I.; Heering, H. A.; Dekker, C.; Lemay, S. G. Carbon Nanotube Biosensors: The Critical Role of the Reference Electrode. *Appl. Phys. Lett.* **2007**, *91*, 093507.
(13) Zhang, G. J.; Zhang, G.; Chua, J. H.; Chee, R. E.; Wong, E. H.; Agarwal, A.; Buddharaju, K. D.; Singh, N.; Gao, Z.; Balasubramanian, N. DNA Sensing by Silicon Nanowire: Charge Layer Distance Dependence. *Nano Lett.* **2008**, *8*, 1066−1070.
(14) Baumgartner, S.; Vasicek, M.; Bulyha, A.; Heitzinger, C. Optimization of Nanowire DNA Sensor Sensitivity Using Self-Consistent Simulation. *Nanotechnology* **2011**, *22*, 425503−425511.
(15) Stern, E.; Steenblock, E. R.; Reed, M. A.; Fahmy, T. M. Label-Free Electronic Detection of the Antigen-Specific T-Cell Immune Response. *Nano Lett.* **2008**, *8*, 3310−3314.
(16) Squires, T. M.; Messinger, R. J.; Manalis, S. R. Making It Stick: Convection, Reaction and Diffusion in Surface-Based Biosensors. *Nat. Biotechnol.* **2008**, *26*, 417−426.
(17) Sheehan, P. E.; Whitman, L. J. Detection Limits for Nanoscale Biosensors. *Nano Lett.* **2005**, *5*, 803−807.
(18) Cui, Y.; Kim, S. N.; Naik, R. R.; McAlpine, M. C. Biomimetic Peptide Nanosensors. *Acc. Chem. Res.* **2012**, *45*, 696−704.
(19) Patolsky, F.; Zheng, G.; Lieber, C. M. Nanowire Sensors for Medicine and the Life Sciences. *Nanomedicine* **2006**, *1*, 51−65.
(20) Henriksson, A.; Friedbacher, G.; Hoffmann, H. Surface Modification of Silicon Nanowires via Copper-Free Click Chemistry. *Langmuir* **2011**, *27*, 7345−7348.
(21) Nuzaihan, M. M. N.; Hashim, U.; Md Arshad, M. K.; Kasjoo, S. R.; Rahman, S. F. A.; Ruslinda, A. R.; Fathil, M. F. M.; Adzhri, R.; Shahimin, M. M. Electrical Detection of Dengue Virus DENV. DNA Oligomer Using Silicon Nanowire Biosensor with Novel Molecular Gate Control. *Biosens. Bioelectron.* **2016**, *83*, 106−114.
(22) Gao, A.; Lu, N.; Wang, Y.; Dai, P.; Li, T.; Gao, X.; Wang, Y.; Fan, C. Enhanced Sensing of Nucleic Acids with Silicon Nanowire Field Effect Transistor Biosensors. *Nano Lett.* **2012**, *12*, 5262−5268.
(23) Hahm, J.; Lieber, C. M. Direct Ultrasensitive Electrical Detection of DNA and DNA Sequence Variations Using Nanowire Nanosensors. *Nano Lett.* **2004**, *4*, 51−54.
(24) Seker, F.; Meeker, K.; Kuech, T. F.; Ellis, A. B. Surface Chemistry of Prototypical Bulk II-VI and III-V Semiconductors and Implications for Chemical Sensing. *Chem. Rev.* **2000**, *100*, 2505−2536.
(25) Nicu, L.; Leichle, T. Biosensors and Tools for Surface Functionalization from the Macro-to the Nanoscale: The Way Forward. *J. Appl. Phys.* **2008**, *104*, 111101.
(26) Park, J. H.; Von Maltzahn, G.; Zhang, L.; Derfus, A. M.; Simberg, D.; Harris, T. J.; Ruoslahti, E.; Bhatia, S. N.; Sailor, M. J. Systematic Surface Engineering of Magnetic Nanoworms for in Vivo Tumor Targeting. *Small* **2009**, *5*, 694−700.
(27) Metwalli, E.; Haines, D.; Becker, O.; Conzone, S.; Pantano, C. G. Surface Characterizations of Mono-, Di-, and Tri-Aminosilane Treated Glass Substrates. *J. Colloid Interface Sci.* **2006**, *298*, 825−831.
(28) Wang, D.; Jones, F. R. ToF-SIMS and XPS Studies of the Interaction of Silanes and Matrix Resins with Glass Surfaces. *Surf. Interface Anal.* **1993**, *20*, 457−467.
(29) Vandenberg, E. T.; Bertilsson, L.; Liedberg, B.; Uvdal, K.; Erlandsson, R.; Elwing, H.; Lundström, I. Structure of 3-Aminopropyl Triethoxy Silane on Silicon Oxide. *J. Colloid Interface Sci.* **1991**, *147*, 103−118.
(30) Zhang, F.; Sautter, K.; Larsen, A. M.; Findley, D. A.; Davis, R. C.; Samha, H.; Linford, M. R. Chemical Vapor Deposition of Three Aminosilanes on Silicon Dioxide: Surface Characterization, Stability, Effects of Silane Concentration, and Cyanine Dye Adsorption. *Langmuir* **2010**, *26*, 14648−14654.
(31) Ebner, A.; Wildling, L.; Kamruzzahan, A. S. M.; Rankl, C.; Wruss, J.; Hahn, C. D.; Hölzl, M.; Zhu, R.; Kienberger, F.; Blaas, D.; et al. A New, Simple Method for Linking of Antibodies to Atomic Force Microscopy Tips. *Bioconjugate Chem.* **2007**, *18*, 1176−1184.
(32) Janissen, R.; Oberbarnscheidt, L.; Oesterhelt, F. Optimized Straight Forward Procedure for Covalent Surface Immobilization of Different Biomolecules for Single Molecule Applications. *Colloids Surf., B* **2009**, *71*, 200−207.
(33) Choi, C.; Hwang, I.; Cho, Y. L.; Han, S. Y.; Jo, D. H.; Jung, D.; Moon, D. W.; Kim, E. J.; Jeon, C. S.; Kim, J. H.; et al. Fabrication and Characterization of Plasma-Polymerized Polyethylene Glycol Film with Superior Biocompatibility. *ACS Appl. Mater. Interfaces* **2013**, *5*, 697−702.
(34) Jain, A.; Liu, R.; Xiang, Y. K.; Ha, T. Single-Molecule Pull-down for Studying Protein Interactions. *Nat. Protoc.* **2012**, *7*, 445−452.
(35) Harris, J. M. *Poly(Ethylene Glycol) Chemistry*; Springer, 1992; Vol. *11*.
(36) Welch, N. G.; Scoble, J. A.; Muir, B. W.; Pigram, P. J. Orientation and Characterization of Immobilized Antibodies for Improved Immunoassays Review. *Biointerphases* **2017**, *12*, 02D301.
(37) Trilling, A. K.; Beekwilder, J.; Zuilhof, H. Antibody Orientation on Biosensor Surfaces: A Minireview. *Analyst* **2013**, *138*, 1619−1627.
(38) Nikolelis, D.; Varzakas, T.; Erdem, A.; Nikoleli, G.-P. Portable Biosensing of Food Toxicants and Environmental Pollutants. *Portable Biosens. Food Toxicants Environ. Pollut.* **2013**, *20135247*, 515−560.
(39) Tian, B.; Xie, P.; Kempa, T. J.; Bell, D. C.; Lieber, C. M. Single-Crystalline Kinked Semiconductor Nanowire Superstructures. *Nat. Nanotechnol.* **2009**, *4*, 824−829.
(40) Moreau, A. L. D.; Janissen, R.; Santos, C. A.; Peroni, L. A.; Stach-Machado, D. R.; de Souza, A. A.; de Souza, A. P.; Cotta, M. A. Highly-Sensitive and Label-Free Indium Phosphide Biosensor for Early Phytopathogen Diagnosis. *Biosens. Bioelectron.* **2012**, *36*, 62−68.
(41) Van de Walle, C. G.; Neugebauer, J. Universal Alignment of Hydrogen Levels in Semiconductors, Insulators and Solutions. *Nature* **2003**, *423*, 626−628.
(42) Joyce, H. J.; Docherty, C. J.; Gao, Q.; Tan, H. H.; Jagadish, C.; Lloyd-Hughes, J.; Herz, L. M.; Johnston, M. B. Electronic Properties of GaAs, InAs and InP Nanowires Studied by Terahertz Spectroscopy. *Nanotechnology* **2013**, *24*, 214006.

DOI: 10.1021/acs.nanolett.7b01803
Nano Lett. XXXX, XXX, XXX−XXX

(43) Rassi, A., Jr; Rassi, A.; Marcondes de Rezende, J. American Trypanosomiasis Chagas Disease. *Infect Dis Clin N Am.* **2012**, *26*, 275−291.
(44) Clayton, J. Chagas Disease 101. *Nature* **2010**, *465*, S4−S5.
(45) Coura, J. R.; Viñas, P. A. Chagas Disease: A New Worldwide Challenge. *Nature* **2010**, *465*, S6−S7.
(46) Ohno, Y.; Maehashi, K.; Yamashiro, Y.; Matsumoto, K. Electrolyte-Gated Graphene Field-Effect Transistors for Detecting Ph and Protein Adsorption. *Nano Lett.* **2009**, *9*, 3318−3322.
(47) Fu, W.; Feng, L.; Mayer, D.; Panaitov, G.; Kireev, D.; Offenhausser, A.; Krause, H. J. Electrolyte-Gated Graphene Ambipolar Frequency Multipliers for Biochemical Sensing. *Nano Lett.* **2016**, *16*, 2295−2300.
(48) Cai, B.; Wang, S.; Huang, L.; Ning, Y.; Zhang, Z.; Zhang, G.-J. Ultrasensitive Label-Free Detection of PNA−DNA Hybridization by Reduced Graphene Oxide Field-Effect Transistor Biosensor. *ACS Nano* **2014**, *8*, 2632−2638.
(49) Reiner-Rozman, C.; Kotlowski, C.; Knoll, W. Electronic Biosensing with Functionalized rGO FETs. *Biosensors* **2016**, *6*, 17.
(50) Lee, D.-W.; Lee, J.; Sohn, I. Y.; Kim, B.-Y.; Son, Y. M.; Bark, H.; Jung, J.; Choi, M.; Kim, T. H.; Lee, C.; et al. Field-Effect Transistor with a Chemically Synthesized MoS2 Sensing Channel for Label-Free and Highly Sensitive Electrical Detection of DNA Hybridization. *Nano Res.* **2015**, *8*, 2340−2350.
(51) Sarkar, D.; Liu, W.; Xie, X.; Anselmo, A. C.; Mitragotri, S.; Banerjee, K. MoS2 Field-Effect Transistor for next-Generation Label-Free Biosensors. *ACS Nano* **2014**, *8*, 3992−4003.
(52) Caserta, R.; Takita, M. A.; Targon, M. L.; Rosselli-Murai, L. K.; de Souza, A. P.; Peroni, L.; Stach-Machado, D. R.; Andrade, A.; Labate, C. A.; Kitajima, E. W.; et al. Expression of *Xylella fastidiosa* Fimbrial and Afimbrial Proteins during Biofilm Formation. *Appl. Environ. Microbiol.* **2010**, *76*, 4250−4259.
(53) Jokerst, J. V.; Lobovkina, T.; Zare, R. N.; Gambhir, S. S. Nanoparticle PEGylation for Imaging and Therapy. *Nanomedicine* **2011**, *6*, 715−728.
(54) Cross, G. H.; Freeman, N. J.; Swann, M. J. Dual Polarization Interferometry: A Real-Time Optical Technique for Measuring (Bio) Molecular Orientation, Structure and Function at the Solid/Liquid Interface. *Handbook of Biosensors and Biochips*; Wiley, 2007; pp 1−20.
(55) Preiner, J.; Kodera, N.; Tang, J.; Ebner, A.; Brameshuber, M.; Blaas, D.; Gelbmann, N.; Gruber, H. J.; Ando, T.; Hinterdorfer, P. IgGs Are Made for Walking on Bacterial and Viral Surfaces. *Nat. Commun.* **2014**, *5*, 4394.
(56) Yang, L.; Li, Y. AFM and Impedance Spectroscopy Characterization of the Immobilization of Antibodies on Indium-Tin Oxide Electrode through Self-Assembled Monolayer of Epoxysilane and Their Capture of Escherichia Coli O157:H7. *Biosens. Bioelectron.* **2005**, *20*, 1407−1416.
(57) Klein, J. S.; Gnanapragasam, P. N. P.; Galimidi, R. P.; Foglesong, C. P.; West, A. P.; Bjorkman, P. J. Examination of the Contributions of Size and Avidity to the Neutralization Mechanisms of the Anti-HIV Antibodies b12 and 4E10. *Proc. Natl. Acad. Sci. U. S. A.* **2009**, *106*, 7385−7390.
(58) Ma, C.; Hou, Y.; Liu, S.; Zhang, G. Effect of Microphase Separation on the Protein Resistance of a Polymeric Surface. *Langmuir* **2009**, *25*, 9467−9472.
(59) Harbers, G. M.; Emoto, K.; Greef, C.; Metzger, S. W.; Woodward, H. N.; Mascali, J. J.; Grainger, D. W.; Lochhead, M. J. Functionalized Polyethylene Glycol.-Based Bioassay Surface Chemistry That Facilitates Bio-Immobilization and Inhibits Nonspecific Protein, Bacterial, and Mammalian Cell Adhesion. *Chem. Mater.* **2007**, *19*, 4405−4414.
(60) Chiaramonte, T.; Tizei, L. H. G.; Ugarte, D.; Cotta, M. A. Kinetic Effects in InP Nanowire Growth and Stacking Fault Formation: The Role of Interface Roughening. *Nano Lett.* **2011**, *11*, 1934−1940.
(61) van Vugt, L. K.; Veen, S. J.; Bakkers, E. P. A. M.; Roest, A. L.; Vanmaekelbergh, D. *J. Am. Chem. Soc.* **2005**, *127*, 12357.
(62) Bao, W.; Melli, M.; Caselli, N.; Riboli, F.; Wiersma, D. S.; Staffaroni, M.; Choo, H.; Ogletree, D. F.; Aloni, S.; Bokor, J.; et al. Mapping Local Charge Recombination Heterogeneity by Multidimensional Nanospectroscopic Imaging. *Science* **2012**, *338*, 1317−1321.
(63) Galtier, N. GC-Content Evolution in Mammalian Genomes: The Biased Gene Conversion Hypothesis. *Dev. Psychobiol.* **2001**, *39*, 251−256.
(64) Amit, M.; Donyo, M.; Hollander, D.; Goren, A.; Kim, E.; Gelfman, S.; Lev-Maor, G.; Burstein, D.; Schwartz, S.; Postolsky, B.; et al. Differential GC Content between Exons and Introns Establishes Distinct Strategies of Splice-Site Recognition. *Cell Rep.* **2012**, *1*, 543−556.
(65) Santos, F. L. N.; Celedon, P. A. F.; Zanchin, N. I. T.; Brasil, T.; Foti, L.; Souza, W. V.; Silva, E. D.; Gomes, Y.; de, M.; Krieger, M. A. Performance Assessment of Four Chimeric *Trypanosoma cruzi* Antigens Based on Antigen-Antibody Detection for Diagnosis of Chronic Chagas Disease. *PLoS One* **2016**, *11*, e0161100.
(66) Stern, E.; Wagner, R.; Sigworth, F. J.; Breaker, R.; Fahmy, T. M.; Reed, M. A. Importance of the Debye Screening Length on Nanowire Field Effect Transistor Sensors. *Nano Lett.* **2007**, *7*, 3405−3409.
(67) Arnold, K.; Herrmann, A.; Pratsch, L.; Gawrisch, K. The Dielectric Properties of Aqueous Solutions of Polyethylene Glycol and Their Influence on Membrane Structure. *Biochim. Biophys. Acta, Biomembr.* **1985**, *815*, 515−518.
(68) Gao, N.; Zhou, W.; Jiang, X.; Hong, G.; Fu, T.-M.; Lieber, C. M. General Strategy for Biodetection in High Ionic Strength Solutions Using Transistor-Based Nanoelectronic Sensors. *Nano Lett.* **2015**, *15*, 2143−2148.
(69) Daniels, J. S.; Pourmand, N. Label-Free Impedance Biosensors: Opportunities and Challenges. *Electroanalysis* **2007**, *19*, 1239−1257.
(70) Lee, H. J.; Wark, A. W.; Corn, R. M. Creating Advanced Multifunctional Biosensors with Surface Enzymatic Transformations. *Langmuir* **2006**, *22*, 5241−5250.
(71) Shrivastava, A.; Gupta, V. Methods for the Determination of Limit of Detection and Limit of Quantitation of the Analytical Methods. *Chronicles Young Sci.* **2011**, *2*, 21.
(72) Narváez, A. C.; Chiaramonte, T.; Vicaro, K. O.; Clerici, J. H.; Cotta, M. a. Evidence of Space Charge Regions within Semiconductor Nanowires from Kelvin Probe Force Microscopy. *Nanotechnology* **2009**, *20*, 465705.
(73) Belluzo, M. S.; Ribone, M. É.; Camussone, C.; Marcipar, I. S.; Lagier, C. M. Favorably Orienting Recombinant Proteins to Develop Amperometric Biosensors to Diagnose Chagas' Disease. *Anal. Biochem.* **2011**, *408*, 86−94.
(74) Duarte, L. F.; Flórez, O.; Rincón, G.; González, C. I. Comparison of Seven Diagnostic Tests to Detect *Trypanosoma cruzi* Infection in Patients in Chronic Phase of Chagas Disease. *Colomb. medica Cali, Colomb.* **2014**, *45*, 61−66.
(75) Https://www.cdc.gov/parasites/chagas/health_professionals/dx.html (accessed on Sept 14, 2017).
(76) Ferreira, A. A. P.; Colli, W.; da Costa, P. I.; Yamanaka, H. Immunosensor for the Diagnosis of Chagas' Disease. *Biosens. Bioelectron.* **2005**, *21*, 175−181.
(77) Regiart, M.; Pereira, S. V.; Bertolino, F. A.; Garcia, C. D.; Raba, J.; Aranda, P. R. An Electrochemical Immunosensor for Anti-*T. cruzi* IgM Antibodies, a Biomarker for Congenital Chagas Disease, Using a Screen-Printed Electrode Modified with Gold Nanoparticles and Functionalized with Shed Acute Phase Antigen. *Microchim. Acta* **2016**, *183*, 1203−1210.
(78) Homola, J. Surface Plasmon Resonance Sensors for Detection of Chemical and Biological Species. *Chem. Rev.* **2008**, *108*, 462−493.
(79) Xu, S.; Zhan, J.; Man, B.; Jiang, S.; Yue, W.; Gao, S.; Guo, C.; Liu, H.; Li, Z.; Wang, J.; et al. Real-Time Reliable Determination of Binding Kinetics of DNA Hybridization Using a Multi-Channel Graphene Biosensor. *Nat. Commun.* **2017**, *8*, 14902.
(80) Duan, X.; Li, Y.; Rajan, N. K.; Routenberg, D. A.; Modis, Y.; Reed, M. A. Quantification of the Affinities and Kinetics of Protein Interactions Using Silicon Nanowire Biosensors. *Nat. Nanotechnol.* **2012**, *7*, 401−407.

DOI: 10.1021/acs.nanolett.7b01803
Nano Lett. XXXX, XXX, XXX−XXX

(81) Arlett, J. L.; Myers, E. B.; Roukes, M. L. Comparative Advantages of Mechanical Biosensors. *Nat. Nanotechnol.* **2011**, *6*, 203−215.

DOI: 10.1021/acs.nanolett.7b01803
Nano Lett. XXXX, XXX, XXX−XXX

InP Nanowire Biosensor with tailored Biofunctionalization: Ultrasensitive and Highly Selective Disease Biomarker Detection

Richard Janissen[1,2,,#], Prasana K. Sahoo[1,‡, #], Clelton A. Santos[3], Aldeliane M. da Silva[1], Antonio A.G. von Zuben[1], Denio E.P.Souto,[4] Alexandre D.T. Costa[5], Paola Celedon[6], Nilson I.T. Zanchin[5], Diogo B. Almeida[1,§], Douglas S. Oliveira[1], Lauro T. Kubota,[4] Carlos L. Cesar[1], Anete P. de Souza[3], Monica A. Cotta[1,*]*

[1] "Gleb Wataghin" Physics Institute, University of Campinas, Campinas, SP, Brazil

[2] Kavli Institute of Nanoscience, Delft University of Technology, 2629 HZ Delft, The Netherlands

[3] Center for Molecular Biology and Genetic Engineering, Biology Institute, University of Campinas, Campinas, SP, Brazil

[4] Chemistry Institute, University of Campinas, Campinas, SP, Brazil

[5] Carlos Chagas Institute, Oswaldo Cruz Foundation, Curitiba, PR, Brazil

[6] Molecular Biology Institute of Paraná, Curitiba, PR, Brazil

Supporting Information

Present Addresses

‡ Department of Physics, University of South Florida, Tampa, FL 33620-7100, USA

§ Department of Physics, University of Michigan, Ann Arbor, MI 48109-1040, USA

1. Material and methods

1.1 Indium Phosphide thin film and nanowire growth

Indium Phosphide (InP) nanowires (NW) were grown on GaAs (001) substrates by chemical beam epitaxy (CBE), using colloidal gold nanoparticles as catalyst material, with an average diameter of 5 nm as described previously[1].The substrate native oxide was not desorbed prior to InP growth. Trimethylindium (TMI) diluted in hydrogen carrier gas and thermally decomposed phosphine (PH3) were used as group III and V sources, respectively. A PH3-flow of 15 sccm and a TMI flow of 0.45 sccm were used for a total growth time of 75 min at 420°C. The samples were inspected by scanning electron microscopy (SEM, FEI Inspect F50). Due to lateral growth at the regions closer to the substrate surface, the nanowires present a conical shape, with a wider base than the apex. Structural characterization of the InP nanowires show that they grow in the wurtzite phase, oriented along the [0001] axis.

InP thin films were grown on semi-insulating, nominally-oriented (001) InP substrates by Chemical Beam Epitaxy. After substrate oxide desorption at 550°C, a PH3-flow of 7.5 sccm and a TMI flow of 0.36 sccm were used for a total growth time of 15 min at 550°C. InP layer thickness was ~140 nm and the residual carrier concentration for the undoped sample $\sim 10^{14}$ cm^{-3}.

1.2 InP Nanowire device fabrication

Prior to the InP nanowire alignment, SiO_2 substrates (1.5 × 1.5 cm) were cleaned with acetone, isopropanol and DI water in that order in an ultrasonic bath for 15 min each, followed by oxygen plasma cleaning for 5 min (200 W, 50 sccm of O_2). A 1-2 μm thick positive photoresist [*AZ® 5214E*] was spin-coated on the SiO_2 substrates (4,000 rpm, 40 s), followed by baking step at 110°C for 2 min. Hexamethyldisilazane (HMDS) was used as an adhesive promoter prior to the *AZ® 5214E* photoresist coating. The electrode positions (see Figure S3) were designed via computer-aided design (AutoCAD, Autodesk, USA), followed by laser lithography process (μPG 101, Heidelberg Instruments Mikrotechnik GmbH, Germany) on the photoresist-coated substrates. Afterwards, the substrates were further developed via *AZ 351B (MIC)* solution, typically used in 1:4 dilution for 60 s. Different metal layer combination of Ti/Ni/Ge/Au (5, 10, 50, 150 nm in thickness, respectively) were then deposited by e-beam evaporation over the patterned substrate followed by a lift-off process in acetone overnight. InP nanowires were mechanically removed from the growth substrate and dispersed in isopropanol by mild ultra-sonication. This well dispersed nanowire containing solution was immediately allowed to flow over the metal electrode arrays (Figure S3) using polydimethylsiloxane (PDMS) microfluidic channels (width: 100 μm; height: 50 μm) with flow rate of 100 μl/min through polyethylene tubing emanating from a syringe pump attached to the inlet of the microfluidic channel. The analyte-exposed regions of the sensor probe were further defined via UV-photolithography, followed by a second layer of metal

deposition (Au, 100 nm thick) as shown in Fig. S1B. An additional UV-photolithography step (inverted pattern of the mask shown in Fig. S1B) was employed in order to passivate the remaining parts of the chip to deposit a 20 nm thick SiNx layer on the unexposed region of the sensor chip. The nanowires were thermally annealed to the electrodes at 430°C for 3 min in N_2 atmosphere for ohmic contact formation. These nanowires were further functionalized with 80b probe DNA or anti-IBMP8-1 antibodies prior to the sensor measurement.

1.3 Scanning electron microscopy and compositional analysis of InP nanowires

InP nanowire growth was evaluated using scanning electron microscopy (SEM) imaging and Energy Dispersive X-Ray Spectroscopy (EDS) in a high-resolution FESEM (Field Emission Scanning Electron Microscopy; FEI Inspect F50, FEI, USA) on GaAs (001) substrates after gentle mechanical abrasion of nanowires from the GaAs growth substrate as reported previously[1]. The nanowire samples were analyzed using low electron beam energy (1 keV) in the secondary electron imaging mode. Adopting the Field Emission Gun (FEG) during FESEM measurements provided high contrast imaging with low electrostatic distortion resulting in a spatial resolution ~ 2 nm.

1.4 InP surface functionalization

DNA-functionalization experiments were carried out for both InP thin films and InP nanowires. Prior to applying the chemical functionalization protocol, the InP thin film samples were cleaned in O_2 plasma (40 W, 100 sccm of O_2) for 10 min. InP nanowires were removed by soft mechanical abrasion from the GaAs substrates. Both samples were incubated in anhydrous DMSO (dimethyl sulfoxide, Sigma, USA) containing 5 M ethanolamine hydrochloride. In case of InP nanowires aligned to the biosensor device surface, the ethanolamine hydrochloride solution was added to the entire chip surface to aminate only the exposed regions of the nanowires. After the incubation for 12 h at room temperature for surface amination, the samples were washed with DMSO, twice with ethanol and finally rinsed with water. After drying in a laminar flow bench, the InP samples were PEGylated by depositing 2 mM of amino-reactive, heterobifunctional NHS-PEG-COOH (MW 3.400, LaysanBio, USA) in water-free chloroform containing 0.5% (v/v) trimethylamine for 1 h at room temperature. After the PEGylation process, the supports were washed five times in water and dried again in a laminar flow bench. For covalent probe DNA attachment, amino-labeled 40b probe DNA oligonucleotides (for surface functionalization characterization; Table S1) or 80b probe DNA (for Kelvin Probe Force Microscopy (KPFM) and biosensor measurements; Table S1) were bound to the PEG-coated substrates via peptide binding using a concentration of 10 pmol μl^{-1} ssDNA in 100 mM MES (2-(N-morpholino)ethanesulfonic acid, Sigma, USA) buffer (pH 4.7) containing 50 mM EDC (1-Ethyl-3-(3-dimethylaminopropyl)-carbodiimide, Sigma, USA) for 1 h reaction time at room temperature. After ssDNA immobilization, the supports were washed twice with water, 10

min in a 10 mM KCl (potassium chloride, Sigma, USA) solution to eliminate unspecific adhered oligonucleotides and finally 5 min in water followed by drying in a laminar flow bench.

The hybridization of the Atto647N-labeled complementary 40b target DNA strand (or non-labelled complementary 80b target DNA for KPFM and biosensor measurements; Table S1) was carried out for 1 h at room temperature in TRIS-HCl buffer (20 mM TRIS, 100 mM NaCl, pH 8.4) and washed afterwards in 2 × SSC (saline-sodium citrate, pH 8.4) buffer for 5 min and in 0.01 × SSC buffer for another 5 min to remove non-specifically adsorbed ssDNA.

To functionalize InP nanowires with antibodies against IBMP8-1, 100 µg/ml polyclonal IBMP8-1 antibodies from the antiserum were covalently bound to previously PEG-coated nanowires via peptide binding for 1 h in 100 mM MES buffer (pH 4.75) containing 50 mM EDC. Afterwards, the substrates were washed twice for 10 min with PBS-T buffer (PBS, 0.05% (v/v) Tween 20, pH 7.4) and once with PBS buffer for 5 min. Specific antibody:antigen binding during *in situ* biosensor titration measurements was carried out adding IBMP8-1 with a following incubation time of 1 h at room temperature. Non-specifically adsorbed IBMP8-1 proteins were removed afterwards by washing the substrates three times for 10 min with PBS-T and twice for 10 min in PBS buffer.

1.5 Cloning, expression and purification of the *Xylella fastidiosa* adhesin Xf.XadA2

The Xf.XadA2 sequence ORF Xf1270 (6177bp) that encodes the *X. fastidiosa* surface adhesion protein Xf.XadA2 (2059 amino acid residues) was amplified by PCR (polymerase chain reaction) from the *X. fastidiosa* genomic DNA. The "head" domain of Xf.XadA2, beginning at residue 730 and ending at residue 900, was designed using the primers XadA2forward (5'-AATCATATGGCTGGTACGGAAGAGAC-3') and XadA2reverse (5'-AAATGAATTCCACGACCGAC TGACC-3'), containing the NdeI and EcoRI restriction enzyme sites, respectively. The PCR amplicon was cloned into the expression vector pET28a(+) (Novagen, USA), which added an N-terminal histidine-tag (containing six histidine) and a thrombin protease site to the coding sequence. The Xf.XadA2 was overexpressed in *Escherichia coli* C43 (DE3) strain (Avidis, Saint-Beauzire, France). Cells were grown at 37°C in 1 liter of LB (Luria-Bertani) medium, supplemented with 0.2% glucose and kanamycin (30 µg/ml) until optical absorbance of OD_{600} of 0.6 – 0.8 was reached. Expression of the recombinant protein was induced by the addition of 1 mM IPTG (isopropyl-β-D-1-thiogalactopyranoside) followed by cultivation for 4 h at 25°C and 200 rpm. The culture was harvested by centrifugation (3.000 g, 15 min, 4°C) and sedimented cells were resuspended in 50 mL of buffer A (50 mM Tris-HCl, 150 mM NaCl, pH 8.0) that contains 1 mg/ml lysozyme and 1 mM phenylmethanelsulfonyl fluoride (Sigma, St Louis, USA). After the incubation on ice for 30 min, the lysates were disrupted by sonication and the unbroken cells and debris were removed by centrifugation (27,000 g, 40 min, 4°C). The Xf.XadA2 protein purification was performed by affinity chromatography using a Nickel-NTA (nitrilotriacetic acid) resin (Qiagen, Hilden, Germany), equilibrated with

buffer A. The purified proteins were eluted with five column volumes of buffer A, containing 250 mM imidazole and the degree of purity was estimated by SDS-PAGE (sodium dodecyl sulfate polyacrylamide gel electrophoresis). After the purification step, the N-terminal His6-tags of recombinant proteins were removed using a thrombin cleavage kit (Novagen, USA).

1.6 Polyclonal Xf.XadA2 antibody production

The *Xylella fastidiosa* polyclonal IgG antibody against Xf.XadA2 (further called anti-Xf.XadA2) was obtained by immunization of New Zealand White Rabbits based on the protocol of Caserta *et al* [2]. Briefly, 150 µg purified Xf.XadA2 proteins were mixed with Freund's complete adjuvant (Sigma, St Louis, USA) and injected into individual rabbits. The proteins solution was injected two more times, at 10 and 20 days after the first injection. The quality of the antibodies was verified by performing a direct ELISA (enzyme-linked immunosorbent assay), using the target Xf.XadA2 proteins as antigens and PBS as the negative control.

1.7 Expression and purification of the IBMP 8-1 protein

IBMP 8-1 sequences were selected from literature and comprises several fragments of *Trypanosoma cruzi* antigenic proteins. Its recombinant production and performance in Chagas disease immunodiagnosis have already been described in a previous study[3]. Briefly, a synthetic gene[3], IBMP 8-1, optimized for *Escherichia coli* expression was purchased from a commercial supplier, already in the pUC57 vector (GenScript, Piscataway-NJ, USA). The gene was subcloned into the expression vector pET28a and expressed in *E. coli* BL21 Star (DE3) cells. Bacterial cell cultures were maintained at 37°C, 200 rpm, in LB-Lennox media[4] until they reached an optical density of OD_{600} = 0.7 – 0.8. Protein expression was induced for 4 h using 0.5 mM of isopropyl β-D-1-thiogalactopyranoside (IPTG). Cells were collected by centrifugation (5,000 rpm, 5 min), suspended in lysis buffer (50 mM Tris-HCl, pH 8.0, 300 mM NaCl, EDTA-free protease inhibitor cocktail (Roche, Switzerland), 0.25 mg/ml lysozyme) and kept on ice for 1 h. Cell disruption was accomplished using a microfluidizer (Microfluidics, Westwood, USA) and the lysate was centrifuged for 15 min at 10,000 g to remove cell debris. IBMP8-1 was purified from the supernatant by nickel column liquid chromatography using a 20 – 500 mM linear gradient of imidazole. Protein concentration was estimated by a fluorometric quantitation (Qubit, Invitrogen, USA).

1.8 GST protein expression and purification

Glutathione S-transferase protein (GST) was expressed in *E. coli* BL21 Star (DE3) using the vector pGEX-4T3 (GE Healthcare, USA). Cell culture and expression induction was carried out using the same conditions as for IBMP 8-1. Phosphate buffer saline (PBS, pH 7.4) containing EDTA-free protease inhibitor cocktail (Roche, Switzerland) and 0.25 mg/ml of lysozyme was used as lysis buffer. GST was purified by affinity chromatography on a Glutathione Sepharose 4B (#17-5132-01, GE Healthcare, USA) column, which was eluted

with 20 mM reduced glutathione in PBS, pH 8.0. GST concentration was estimated by Bradford protein assay.[5]

1.9 Production of a polyclonal antibodies against the recombinant IBMP 8-1 protein

Polyclonal antibodies against IBMP8-1 were obtained from the antiserum generated from New Zealand rabbits (age: 3 months) after immunization with the recombinant protein IBMP 8-1 (Rheabiotech, Brazil). The rabbits were subcutaneously immunized using an emulsion of IBMP8-1 with complete Freund's Adjuvant (CFA) initially, followed by Incomplete Freund's Adjuvant (IFA) for all subsequent injections. Day 0: 200 µg of antigen in CFA, day 10: 250 µg of antigen in (IFA), day 28: 300 µg of antigen in (IFA), day 35: 400 µg of antigen in (IFA), day 42: final bleed. On day 0 the pre-immune serum was also collected. The polyclonal antiserum quality was verified via indirect ELISA using IBMP8-1 protein for plate sensitization (5 µg/ml) and pre–immune serum as negative control.

1.10 Fluorescence microscopy and optical spectroscopy

The samples were measured using an epifluorescence microscope (Nikon TE2000U, USA) with a peltier-cooled back-illuminated EMCCD camera (IXON3, 1024×1024 pixels, Andor, Ireland) for sensitive fluorescence detection in combination with an 100× oil-immersion objective (CFI APO TIRF, NA. 1.45, Nikon, USA). Fluorophore excitation was achieved by a 150 W mercury-vapor lamp combined with specific filter sets (AHF, Tübingen, Germany) according to the excitation and emission wavelengths of the different fluorophores used in this study (Filter sets F41-054 for Alexa488 and F41-008 for Alexa633 and Atto647N). For each sample the fluorescence intensity (in photon counts s^{-1}) was measured by taking the average over ≥ 10 areas of 10 × 10 µm. Each experiment was repeated three times to test the reproducibility and for statistical distribution.

The photoluminescence spectra of DNA-functionalized InP nanowires in presence and absence of the Atto647N-labeled complementary DNA strand were acquired using an upright confocal laser scanning microscope (LSM780-NLO, Zeiss, Germany) with 633 nm laser excitation using an 63× objective (C-Apochromat, N.A. 1.2, Zeiss, Germany). The signal was sent through a set of dichroic mirror and filters to an external spectrometer (SP2300i, Acton Research Corporation, USA) coupled to a peltier-cooled CCD camera (PIXIS 100BR, Princeton Scientific Instruments, USA). A 150 µm slit aperture and grating of 1,200 g/mm, blazed at 700 nm, was used in the experiments.

1.11 Non-specific biomolecule adhesion and ligand binding efficiency evaluation

Widefield fluorescence microscopy was used to evaluate qualitatively and quantitatively i) the surface coverage of (3-Aminopropyl)triethoxysilane (APTES, Sigma, USA) and ethanolamine hydrochloride (EA, Sigma, USA), ii) the non-specific adhesion of DNA, peptides and proteins on different chemical surface compositions and iii) the binding efficiency of

protein ligands in absence and presence of an additional poly(ethylene glycol) crosslinker. For those experiments, 24 × 24 mm borosilicate cover glasses (Menzel GmbH, Germany) were cleaned and functionalized. To do so, the supports were incubated in a 5% (v/v) aqueous Hellmanex II-solution (Hellma GmbH, Germany) and sonicated for 20 min at 40°C. Afterwards, the samples were washed thoroughly with deionized (DI) water and sonicated again for 20 min in DI water. The supports were then dried in a nitrogen flow and the generation of hydroxyl-groups was carried out applying oxygen plasma (SE80, Barrel Asher Plasma Technology, USA) for 15 min (50 sccm O2, 200 W, 100 mTorr). For the surface coating quality comparison, APTES and EA were grafted covalently to the treated cover glasses and coated with carboxyl-labeled Alexa633 fluorophore (Rheabiotech, Brazil).

The silanization was performed by adding 10 µl of pure APTES between two glass slides and incubation for 15 min at 75°C. The silanized supports were then rinsed thoroughly with ethanol, DI water and dried in a nitrogen flow. The EA coating was performed in the same way as described for presented nanowire functionalization (section 1.4). The covalent peptide-binding between the primary amino groups (of APTES and EA) and the carboxylic group of 10 µM Alexa633 fluorophore was carried out for 1 h in 100 mM MES buffer (pH 4.75) containing 50 mM EDC at room temperature and protected from light. The supports were then washed for 5 min with DI water, 10 min in a 100 mM KCl solution and again 5 min with DI water followed by drying in nitrogen flow. The non-specific adhesion of ssDNA, peptide and protein was tested on coated glass slides with APTES, EA and the addition of the PEG crosslinker used in this study. On each surface coating, a concentration of 10 µM of the different biomolecules was added for 1 h at room temperature. In detail, Atto647N-labeled 40b target DNA was given to the different surface compositions in TRIS/HCl hybridization buffer (20 mM TRIS, 100 mM NaCl, pH 8.4). After 1 h incubation, the surfaces were washed twice for 5 min with the hybridization buffer. As peptide, a custom-synthesized 16 amino acid (N-GGSGSGHHHHHHHHHH-C) construct (Biomedizinisches Forschungszentrum, Heinrich-Heine-University, Germany), labeled with Alexa488 at the C-terminus, was added to the surfaces in PBS buffer (pH 7.4) for 1 h. After incubation, the surfaces were washed twice for 5 min with PBS. A secondary anti-rabbit IgG antibody, labeled with Alexa633 or Alexa488 (Rheabiotech, Brazil), was used as a protein representative in this comparison experiment. The concentration, surface incubation and washing procedures were performed with PBS buffer with the same methodology as used for the peptide incubation. To evaluate the dependence of protein binding efficiency on the spatial distance to the surface, 100 µg/ml polyclonal anti-Xf.XadA2 antibodies were covalently bound to EA only and PEG-coated surfaces for 1 h in 100 mM MES buffer (pH 4.75) containing 50 mM EDC. After washing twice for 10 min with PBS-T buffer (PBS, 0.05% (v/v) Tween 20) and PBS buffer for 5 min, the surfaces were passivated with 3% (m/v) BSA (bovine serum albumin, Sigma, USA) in PBS buffer for 1 h at 37°C. After washing twice for 5 min with PBS, 10 µM of Xf.XadA2 protein was added and incubated for 1 h at 37°C. Followed by washing twice with PBS-T for 10 min and once with PBS for 5 min, 10 µg/ml anti-Xf.XadA2 was incubated again for 1 h at 37°C. Again,

the supports were washed twice with PBS-T for 10 min and PBS for 5 min. For fluorescence detection, 5 µg/ml goat anti-rabbit Alexa633 or Alexa488-conjugated secondary IgG antibodies were added for 1 h at 37°C and protected from light. In a final step, the substrates were washed three times for 10 min with PBS-T and afterwards twice for 10 min in PBS buffer.

1.12. Atomic Force and Kelvin Probe Force Microscopy

Atomic Force Microscopy (AFM) was performed with an Agilent (now Keysight) 5500 equipment, using the MAC III Module with three lock-in amplifiers. In order to investigate protein-functionalized surface layers, the Agilent 5500 model was used to scratch the surface at high forces (≥ 2 nN) using Bruker MLCT silicon nitride cantilevers with a nominal spring constant of ~0.6 N/m and resonance frequency of ~125 kHz. Topography and phase images at the edge of the protein-functionalized surface were acquired to measure the layer height.

Functionalized InP thin films were also characterized by AFM as well as Amplitude Mode Kelvin Probe Force Microscopy (AM-KPFM), using the same equipment and Pt-Ir metallized silicon cantilever tips (Bruker SCM-PIT, nominal spring constant of ~2.8 N/m and 75 kHz resonance frequency). During these measurements, topography, phase and SP images were obtained simultaneously under N_2 atmosphere to reduce the effects of oxidation or water adsorption on the surface. In order to exclude tip wear effects and accurately measure surface potential variations, it is important to have a reference material within the imaging window of the sample. However, functionalized samples generally presented homogeneous surfaces. Therefore, a sample of InP thin film, which was cleaned with O_2 plasma oxygen plasma (40 W, 100 sccm of O_2) for 10 min, was used as AM-KPFM reference. Measurements were acquired in three different regions, in the reference and subsequently in the functionalized samples, keeping the same microscope settings. Variations in the average SP were thus calculated for each sample, considering the reference SP value for each set of measurements.

1.13 *In-situ* nanowire biosensor titration experiments

The ohmic character of nanowire-electrode bonding on the sensor chip was examined using a self-build probe station and a Semiconductor Characterization System SCS4000 (Keithley, USA). The nanowire sensor chip was mounted on a chip-carrier (with 68 metal pads) using double-sided conductive carbon tape. Using wire bonding (West Bond, USA, model 747677E), Au wires were connected between contact pads and the nanowire containing chip carrier. Once the chip is fixed with the contact pad, a PDMS microfluidic device with four channels (each channel with a width of 100 µm and 50 µm in height) was clamped on the chip carrier such that the individual channels overlap the regions of the sensor chip that contain 16 InP nanowires (Figure S3). Each channel covering the nanowire devices was functionalized with ethanolamine and PEG, to which 80b probe DNA or anti-IBMP8-1

antibodies were further covalently coupled, as described in the sections 1.4 and 1.11. Prior to the in-situ measurement, each channel containing nanowire devices was calibrated in aqueous buffer solutions (DNA: 20 mM TRIS, 100 mM NaCl, pH 8.4; IBMP8-1: PBS, pH 7.4) for 30 min. Titration experiments of complementary 80b target ssDNA (or specific IBMP8-1 target) to 80b probe DNA (or anti-IBMP8-1-coated nanowires) were performed by injecting 50 µl of different biomolecule concentrations (ranging from 10 fM to 1 nM) and measurements were carried out at different interval of times.

During the titration of each different target analyte concentration (DNA, IBMP8-1), the sensor response was recorded up to 60 min. After signal saturation, the target analytes were removed gently by washing three times the appropriate buffer, flushing out by that all unspecific-adhered biomolecules; the in-situ measurements were performed directly after. Simultaneous I-V measurements were performed within voltage range of ± 200 mV. The change in resistance as a function of target DNA/IBMP8-1 protein concentrations was then plotted. To access quantitatively the degree of non-specific adhesion of unspecific target molecules (in case of DNA: 80b probe DNA; for IBMP8-1: GST), titration experiments were performed in the same procedure as described before for the correct target molecules, using the same biomolecule concentrations during their titration.

1.14 *In-situ* Surface Plasmon Resonance titration experiments

The Surface Plasmon Resonance (SPR) technique is a valuable tool to obtain information about the binding rate and the extent of adsorption for biomolecular interactions. Here, real-time SPR sensor responses of IBMP8-1 adsorption at different concentrations were measured (Figure S6; Table S3). For the SPR measurements, an Autolab Spirit instrument (Eco Chemie B. V., Ultrech, The Netherlands) was used. The optical system consists of a glass prism and a planar gold disk, which were both obtained from Xantec Bioanalytics (Muenster, Germany). The system is equipped with a quartz cuvette and a laser diode with a 670 nm wavelength, and its operation mode is based on the Kretschmann configuration. For preparation of the sensor, self-assembled monolayers (SAM) were formed on the gold surface followed by immobilization of anti-IBMP8-1 antibodies. For the functionalization step, the SPR gold substrates were cleaned in piranha solution (1:3 mixture of 30% H_2O_2 and concentrated H_2SO_4) for approximately 3 min, followed by immersion in acetone and in isopropyl alcohol for 5 min each. Afterward, the substrates were washed several times with deionized water and dried under pure N_2 flow. The SAM was formed on the SPR planar gold disk substrate by the incubation in 1 mM 11-mercaptoundecanoic acid (11-MUA) in ethanol during 24 h at room temperature. Then, the substrate was thoroughly washed with ethanol, water, and finally dried under pure N_2 flow. For the covalent attachment of the anti-IBMP8-1 antibodies, the same methodology was used as described for the nanowire biosensor in section 1.4. *In-situ* IBMP8-1 titration experiments were carried out in real time. First, a sensor baseline was established by adding PBS buffer (pH 7.4) and measuring over 200 s. Afterwards, the sensor

response ($\Delta\theta_{SPR}$) was monitored for each IBMP8-1 concentration until saturation (Figure S6B). Successive wash cycle with PBS buffer after saturation assured removal of unbounded IBMP8-1 molecules from the surface. The analysis of the binding kinetics data was performed in the same way as applied for the nanowire biosensor data (section 1.15).

1.15 Analysis of *in-situ* biosensor titration data

The chemical reaction upon free ligand *L* binding to surface-immobilized receptors *R* in a 1:1 binding model can be expressed by:

$$[L] + [R] \leftrightarrow [LR] \tag{1}$$

The expression (1) can be rearranged to calculate the kinetic equilibrium association constant K_A:

$$K_A = \frac{1}{K_D} = \frac{[LR]}{[L][R]} \quad , \tag{2}$$

where K_A and K_D are the equilibrium association and dissociation constants, respectively. To extract the equilibrium dissociation constant K_D from the biosensor data (Figure 5; Figure S6; Table S3), a linear form of Langmuir isotherm[6-9] was used, introducing the changes Δq in resistance (nanowire biosensor) or $\Delta\Theta_{SPR}$ in millidegrees (Surface Plasmon Resonance biosensor) upon ligand adsorption:

$$\frac{[L]}{\Delta q} = \frac{[L]}{\Delta q_{max}} + \frac{K_D}{\Delta q_{max}} \quad , \tag{3}$$

where Δq_{max} is the saturated change in adsorption of ligand *L*. To estimate the association constant K_A, we can calculate either $K_A = \frac{1}{K_D}$, or fit the biosensor responses to a rearranged Langmuir equation expression:

$$\Delta q = \Delta q_{max} \frac{K_A\,[L]}{1 + K_A\,[L]} \, . \tag{4}$$

The limit of detection (LOD) that describes the lowest concentration of the analyte that can be detected by the biosensors, was performed by considering the calibration measurements prior to the biomolecule titration measurements. The LOD was calculated after the Langmuir adsorption isotherm fitting, taken into account the linear slope that corresponds to the biosensor sensitivity for each biomolecule system tested:[10]

$$LOD = \frac{a\ \sigma}{m}\ , \qquad (5)$$

where a = 3 renders a 99.7% confidence interval with 3 × σ, σ = standard deviation of calibration measurement and m = linear slope of the Langmuir adsorption isotherm.

References

1 T. Chiaramonte, L.H. G. Tizei, D. Ugarte and M.A. Cotta, *Nano Letters,* 2011, **11**, 1934-1940.

2 R. Caserta, M.A. Takita, M.L. Targon, L.K. Rosselli-Murai, A.P. de Souza, L. Peroni, D.R. Stach-Machado, A. Andrade, C.A. Labate, E.W. Kitajima, M.A. Machado, A.A. de Souza, *Applied and Environmental Microbiology,* 2010, **76(13)**, 4250-4259.

3 F.L. Santos, P.A. Celedon, N.I. Zanchin, T. de A. Brasil, L. Foti, W.V. Souza, E.D. Silva, Y. de M. Gomes, M.A. Krieger, *PLoS One*, 2016, **11(8)**:e0161100.

4 E.S. Lennox, *Virology*, 1955, **1(2)**: 190–206

5 M. Bradford, *Anal. Biochem*., 1976, **72**, 248–254.

6 H.J. Lee, A.W. Wark, R.M. Corn, *Langmuir,* 2006, **22(12)**, 5241-5250.

7 J.S. Daniels, N. Pourmand, *Electroanalysis,* 2007, **19(12)**, 1239-1257.

8 N. Gao, W. Zhou, X. Jiang, G. Hong, T.-M. Fu, C.M. Lieber, *Nano Lett*., 2015, **15**, 2143-2148.

9 C. Reiner-Rozman, C. Kotlowski, W. Knoll, *Biosensors*, 2016, **6(2)**, 17-29.

10 A. Shrivastava, V. Gupta, *Chron. Young. Sci*., 2011, **2**, 21-25.

11 Y. Ohno, K. Maehashi, Y. Yamashiro, K. Matsumoto, *Nano Lett.,* 2009, **9**, 3318–3322.

12 W. Fu, L. Feng, D. Mayer, G. Panaitov, D. Kireev, A. Offenhausser, H.J. Krause, *Nano Lett.,* 2016, **16**, 2295–2300.

13 B. Cai, S. Wang, L. Huang, Y. Ning, Z. Zhang, G-J. Zhang, *ACS Nano* 2014, **8**, 2632–2638.

14 C. Reiner-Rozman, C. Kotlowski, W. Knoll, *Biosensors,* 2016, **6**, 17.

15 D-W. Lee, J. Lee, I.Y. Sohn, B-Y. Kim, Y.M. Son, H. Bark, J. Jung, M. Choi, T.H, Kim, C. Lee, *et al., Nano Res.,* 2015, **8**, 2340–2350.

16 D. Sarkar, W. Liu, X. Xie, A.C. Anselmo, S. Mitragotri, K. Banerjee, *ACS Nano,* 2014, **8**, 3992–4003.

17 S. Upadhyay, R. Frederiksen, N. Lloret, L. De Vico, P. Krogstrup, J.H. Jensen, K.L. Martinez, J. Nygard, *Appl. Phys. Lett.,* 2014, **104**, 203504.

18 C. Maedler, D. Kim, R.A. Spanjaard, M. Hong, S. Erramilli, P. Mohanty, *ACS Sensors,* 2016, **1**, 696–701.

19 J. Hahm, C.M. Lieber, *Nano Lett.,* 2004, **4**, 51–54.

20 X.P.A. Gao, G. Zheng, C.M. Lieber, *Nano Lett.,* 2010, **10**, 547–552.

21 M.M.N. Nuzaihan, U. Hashim, M.K. Arshad, S.R. Kasjoo, S.F.A. Rahman, A.R. Ruslinda, M.F.M. Fathil, R. Adzhri, M.M. Shahimin, *Biosens. Bioelectron.,* 2016, **83**, 106–114.

22 A. Gao, N. Lu, Y. Wang, P. Dai, T. Li, X. Gao, Y. Wang, C. Fan, *Nano Lett.,* 2012, **12**, 5262–5268.

23 R.D. Blake, J.W. Bizzaro, J.D. Blake, G.R. Day, S.G. Delcourt, J. Knowles, K.A. Marx, J. SantaLucia Jr., *Bioinformatics*, 1999, **15**, 370-375.

24 R. Metzler, T. Ambjörnsson, *J. Biol. Phys*., 2005, **31**, 339-350.

25 J.P. Rasmussen, C.P. Saint, P.T. Monics, *BMC Bioinformatics*, 2007, **8**, 107-118.

26 J. SantaLucia Jr., *Proceedings of the National Academy of Science USA*, 1998, **95**, 1460-1465.

2. Supporting figures

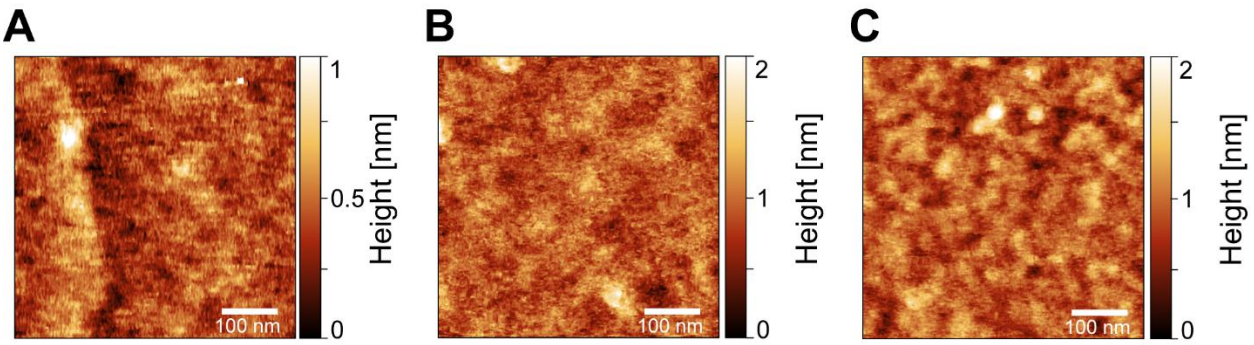

Figure S1. AFM **t**opography of samples of KPFM reference sample (**A**), with 80b probe DNA (**B**), and 10 µM complementary 80b target DNA (**C**). Refers to Figure 2.

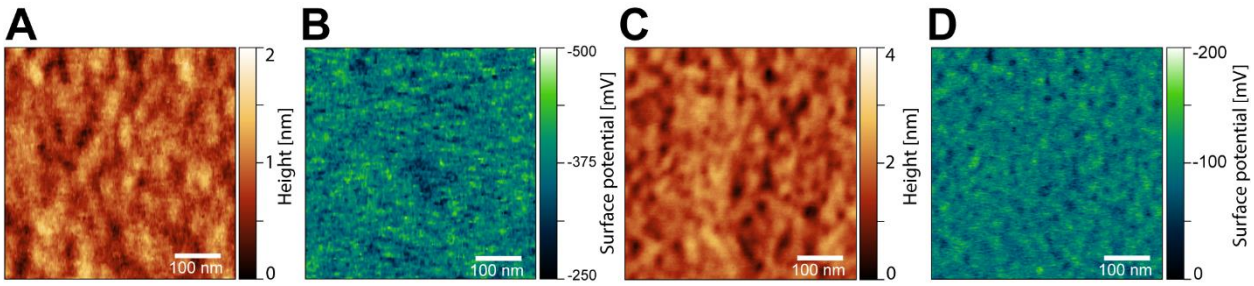

Figure S2. Measured AFM topography and surface potential for samples with added 10 µM complementary 80b target DNA after 30 min (**A**, **B**) and 2 h (**C**, **D**) of drying in N_2 gas**.** Refers to Figure 2.

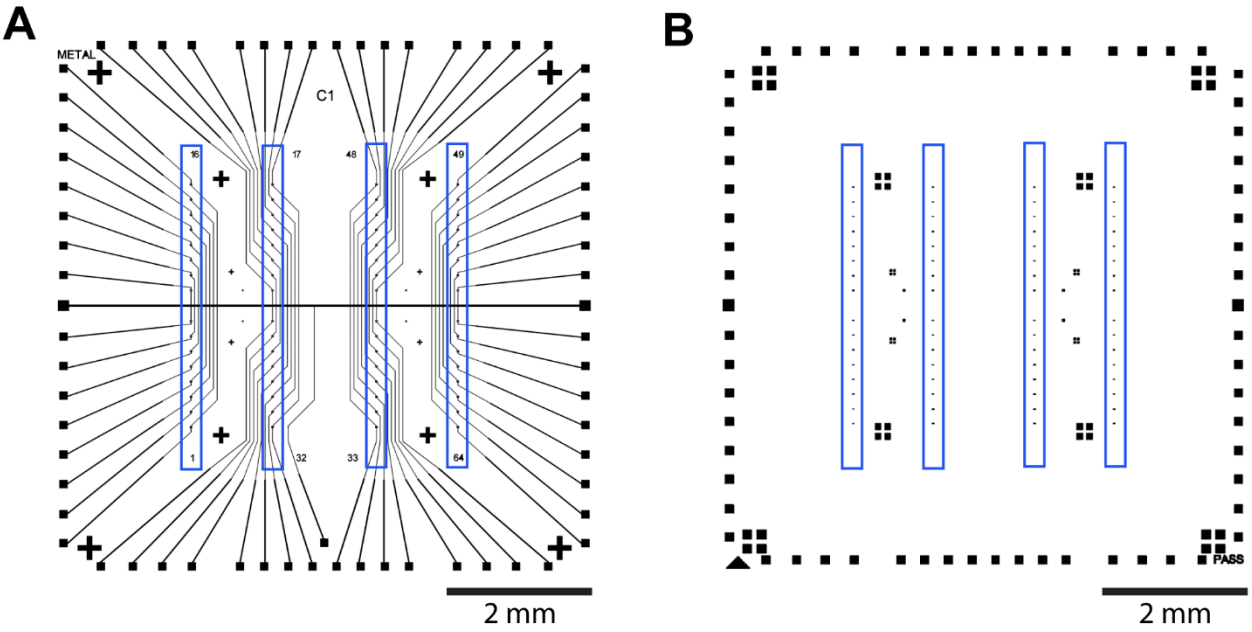

Figure S3. Sensor chip (**A**) with the overlay of four microfluidic channels (indicated by blue rectangles); each channel encompasses 16 electrodes. (**B**) Passivation mask for selective surface functionalization of the sensor chip. Refers to Figure 4.

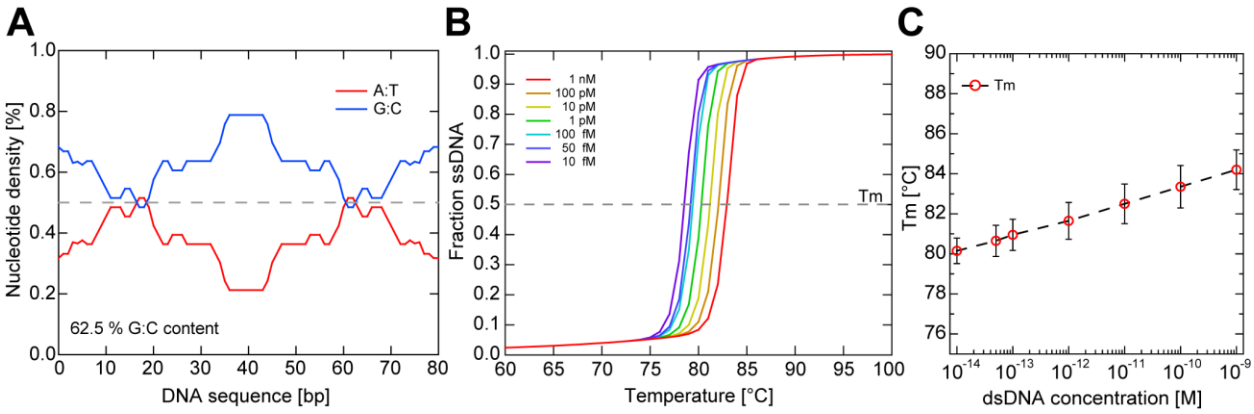

Figure S4. Nucleotide density and thermodynamic stability of 80 bp biosensor sample DNA. (**A**) G:C and A:U basepair content of 80 bp sample DNA. (**B**) Simulated melting curves of 80 bp sample DNA at different concentrations used during *in-situ* titration experiments, based on thermodynamic nearest-neighbor parameters from MeltSim[22-25] and SantaLucia *et al.* 1998[26]. (**C**) Melting temperatures (*Tm*) values obtained for the 80 bp sample DNA at different concentrations. Refers to Figures 3 and 6.

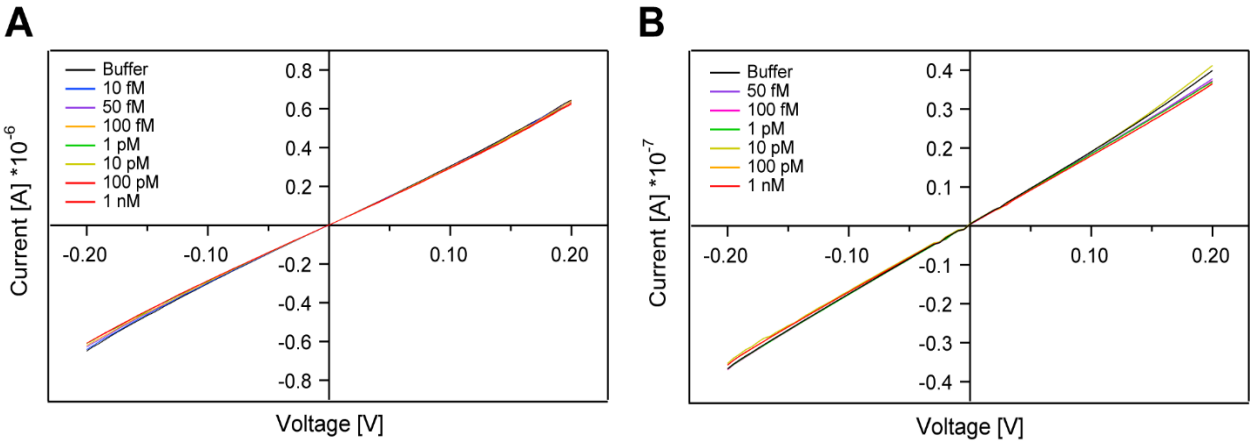

Figure S5. Electrical biosensor I-V response curves upon titration of (**A**) non-complementary 80b probe DNA and (**B**) non-specific GST protein, serving as negative control biomolecules. Refers to Figure 5.

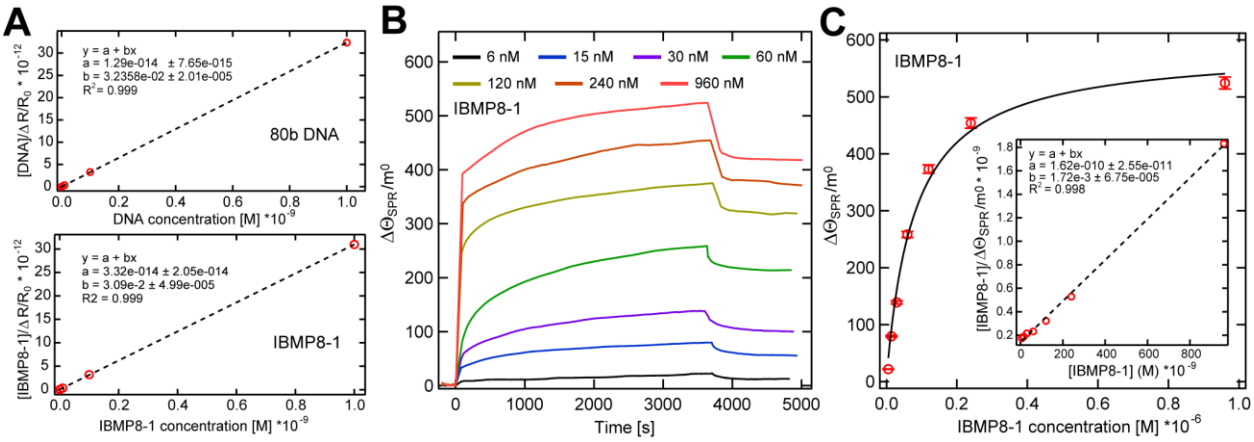

Figure S6. Analysis of InP nanowire biosensor and Surface Plasmon Resonance adsorption data. (**A**) Dissociation equilibrium constant K_D extracted for 80b DNA and IBMP8-1 from linear regression of Langmuir isotherms shown in Figure 5. (**B**) Real-time Surface Plasmon Resonance (SPR) sensor response of IBMP8-1 adsorption at different concentrations. (**C**) Equilibrium SPR IBMP8-1 adsorption values from (B) fitted to Langmuir adsorption isotherm and linear regression (inset) to extract the equilibrium dissociation constant K_D. Refers to Figure 5.

3. SUPPORTING TABLES

Table S1. ssDNA sequences used for surface functionalization characterization and nanowire biosensor measurements (Purimex, Germany).

Name	ssDNA Sequence (5' → 3')
40b probe	NH_2-CCACTCGTGACGCATTCACCTCAGCAGCACTCCTCCTCGG
40b target	Atto647N-CCGAGGAGGAGTGCTGCTGAGGTGAATGCGTC ACGAGTGG
80b probe	NH2- AAAAAAAAAAGGTGAGCACTGCGTAAGTGGAGTCGTCGTGAGGAGGAGCCC CGA GGAGGAGTGCTGCTGAGGTGAATGCGTCACGAGTGG
80b target	CCACTCGTGACGCATTCACCTCAGCAGCACTCCTCCTCGGGGCTCCTCCTCAC GACGACTCCACTTACGCAGTGCTCACC

Table S2. Limit of detection concentrations (LOD) and minimal specific detection concentrations (MCD) of biomolecule detection key studies of different electrical biosensor transducer materials, label-free sensor designs in FET configuration, and Surface Plasmon Resonance sensor used in this work.

Transducer Material	LOD DNA	LOD Protein	MCD DNA	MCD Protein
InP nanowire (*this work*)	1.4 fM	5.7 fM	7 fM	32 fM
Graphene[10,11]	4 pM	100 nM	---	---
Graphene oxide[13,14]	100 fM	100 pM	---	---
$MoSe_2$[15,16]	10 fM	100 fM	---	---
InAs nanowire[17]	---	10 pM	---	---
Si nanowire[18,19]	60 fM	---	---	200 pM
Si nanowire (gate modulation)[20,21,22]	0.1 fM	2 fM	---	---
SPR (*this work*)	---	1.7 nM	---	---

Table S3. Kinetic equilibrium binding constants for IBMP8-1 and 80b DNA adsorptions, extracted from Langmuir isotherms (Figure 5, Figure S6).

	SPR IBMP8-1	Nanowire IBMP8-1	Nanowire 80b DNA
Dissociation constant K_D	1.3×10^{-9} M	1.1×10^{-12} M	4×10^{-13} M
Association constant K_A	7.9×10^{8} M^{-1}	9.3×10^{11} M^{-1}	2.5×10^{12} M^{-1}